Fractional-Step Finite Difference Schemes for Incompressible Elasticity on Overset Grids

J. W. Banks[a], W. D. Henshaw[a,1], A. Newell[a,2,1], D. W. Schwendeman[a,1,*]

[a]*Department of Mathematical Sciences, Rensselaer Polytechnic Institute, Troy, NY 12180, USA*

Abstract

Efficient finite-difference schemes for the numerical solution of the time-dependent equations of incompressible linear elasticity on complex geometry are presented. The schemes are second-order accurate in space and time, and solve the equations in displacement-pressure form. The algorithms use a fractional-step approach in which the time-step of the displacements is performed separately from the solution of a Poisson problem to update the pressure. Complex geometry is treated with curvilinear overset grids. Compatibility boundary conditions and an upwind dissipation for wave equations in second-order form are included to ensure stability for overset grids, and for the difficult case of traction (free-surface) boundary conditions. A divergence damping term is added to keep the dilatation small. The stability of the schemes is studied with GKS mode analysis. Exact eigenmode solutions are obtained for several problems involving rectangular, cylindrical and spherical configurations, and these are valuable as benchmark problems. The accuracy and stability of the approach in two and three space dimensions is illustrated by comparing the numerical solutions with the exact solutions of the benchmark problems.

Keywords: incompressible elasticity; fractional-step methods, overset grids.

Contents

*Department of Mathematical Sciences, Rensselaer Polytechnic Institute, 110 8th Street, Troy, NY 12180, USA.
Email addresses: banksj3@rpi.edu (J. W. Banks), henshw@rpi.edu (W. D. Henshaw), newela5@rpi.edu (A. Newell), schwed@rpi.edu (D. W. Schwendeman)

[1]Research supported by the National Science Foundation under grants DMS-1519934 and DMS-1818926.
[2]Research supported by the National Science Foundation Graduate Research Fellowship under Grant No. DGE-1744655.

1. Introduction

The elastic response of a variety of solid materials can be effectively modeled as incompressible. Such materials include rubber and soft tissue in biological systems [1], among others. In this article we consider the numerical solution of the time-dependent equations of incompressible linear elasticity (ILE). The approach taken here is similar in form to the fractional-step schemes we have developed for the incompressible Navier-Stokes equations [2–4]. In each time-step, these fractional-step schemes advance the fluid velocity followed by an update of the fluid pressure from the solution of a Poisson problem. This basic approach is adopted here for the equations of ILE, but there are some fundamental differences. A key difference is that the underlying dynamics ILE is that of wave propagation, in contrast to incompressible fluids described by the Navier-Stokes equations which are fundamentally advection-diffusion equations. The lack of any natural dissipation in the elasticity equations makes them susceptible to numerical instabilities, and thus significant care is required in designing schemes that remain stable and accurate. Indeed it is well known that finite difference schemes for the displacement form of the nearly incompressible or incompressible linear elastic equations are often unstable at traction (free-surface) boundaries unless special care is taken [5].

Various finite difference schemes for time-dependent compressible elasticity have been developed based on the summation by parts approach [6–9], including schemes that can treat mesh refinement boundaries [10, 11]. Finite volume schemes for time-dependent incompressible elasticity have been developed such as [12], see also the review article [13]. Numerous finite element methods (FEM) have also been developed for time-dependent incompressible or nearly incompressible elasticity. Finite-element approximations for the second-order form of the ILE equations traditionally solve the equations in displacement-divergence form. The resulting saddle-point problem requires some care in its approximation to overcome the problem of *locking* [14]. Mixed methods [15], stabilized methods [16], and Discontinuous Galerkin methods [1], are among the FEM approaches that have been developed that do not suffer from locking. For finite-difference or finite-volume approximations of the incompressible equations, it is natural to consider a projection-type scheme whereby the displacement is first advanced using the momentum equation and then the divergence free condition is enforced by solving a Poisson equation for the pressure correction. The resulting fractional-step scheme can have a significant gain in efficiency. However, some care is required to define boundary conditions in both steps to maintain accuracy, as well as the more difficult requirement of stability with traction boundaries.

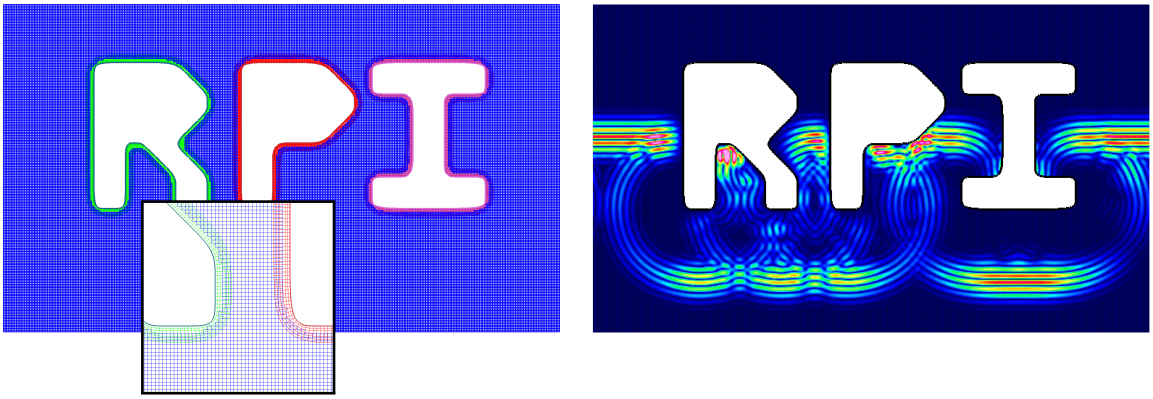

Figure 1: Scattering of a modulated Gaussian plane wave computed using the new SOS-ME-scheme for incompressible elasticity. Left: overset grid for the letters R, P and I, with a magnified view showing the boundary fitted curvilinear grids. Right: contours of the norm of the displacement, $|\mathbf{u}|$.

The present work is motivated by the solution of fluid-structure interaction (FSI) problems on deforming overset grids [17–24]. FSI simulations require schemes that remain accurate up to and including the boundaries, and thus we study the accuracy of approximations not just in terms of L_2-norm errors, but also point-wise (max-norm) errors. In the present article we develop fractional-step schemes for the ILE equations on complex geometry that use overset grids. To the best of our knowledge, this manuscript describes the first stable fractional-step schemes for the solving the ILE equations on overset grids. Figure 1, for example, shows a sample overset grid simulation using the SOS-ME scheme developed in this article. Overset grids present challenges to constructing schemes with discrete energy estimates due to the presence of the overlapping grid boundaries. Thus, we instead investigate an approach that uses compatibility boundary conditions together with upwind dissipation, the latter having recently been developed successfully for wave equations on overset grids [25–27]. Upwind dissipation and compatibility boundary conditions are both critical components of our approach, and the resulting schemes are found to be stable and accurate even with traction boundary conditions. We describe two fractional-step schemes, each with a set of strengths that may make it more appropriate for a particular application area or researcher. The first, denoted by SOS-ME, is a single-step scheme that solves the displacement-pressure formulation in second-order form in space and time (SOS). The SOS-ME scheme has a large CFL-one time-step[3] and is based on a modified equation (ME) time-stepping algorithm as commonly used for wave propagation problems [10, 11, 26, 27]. The second scheme is called FOT-PC, which is a method-of-lines predictor-corrector approach that solves the equations written as a first-order system in time (FOT) for the displacement and velocity. Our FSI schemes often use predictor-corrector formulations, and it is therefore envisioned that the FOT-PC scheme will be useful in this context. For both SOS-ME and FOT-PC, a pressure Poisson problem is solved at each time step using suitable boundary conditions that lead to full second-order accuracy. These new schemes avoid the difficulties associated with the saddle point system, enable high-order accuracy on complex geometry, and avoid splitting errors associated with some projection methods.

The subsequent sections of the article are organized as follows. The governing equations and boundary conditions are presented in Section 2. Section 3 describes the SOS-ME and FOT-PC fractional-step schemes, as well as the discrete approximations to boundary conditions and upwind dissipation. Time-step determination and stability analyses are covered in Section 4, while a discussion of discretizations on overset grids is given in Section 5. Numerical results are presented in Section 6, including derivation of exact solutions for a variety of geometries. These exact solutions, and their development, are one of the contributions of this manuscript which may help future researchers to verify our results or to benchmark their own algorithms. Finally, concluding remarks are given in Section 7.

2. Governing equations

Consider the solution of an initial-boundary-value (IBVP) problem for the equations of incompressible linear elasticity in n_d space dimensions for a domain $\mathbf{x} \in \Omega \subset \mathbb{R}^{n_d}$ and for time $t > 0$. The governing equations in *displacement-divergence* form are

$$\rho\, \partial_t^2 \mathbf{u} = \nabla \cdot \underline{\underline{\boldsymbol{\sigma}}}, \qquad \mathbf{x} \in \Omega, \quad t > 0, \tag{1a}$$

$$\nabla \cdot \mathbf{u} = 0, \qquad \mathbf{x} \in \Omega, \quad t > 0, \tag{1b}$$

[3] A CFL-one time-step is the largest time-step, Δt, normally attainable by an explicit scheme, given by formula (36).

where $\mathbf{u}(\mathbf{x},t)$ is the displacement vector, $\underline{\underline{\boldsymbol{\sigma}}}(\mathbf{x},t)$ is the stress tensor and ρ is the density, the latter taken here to be constant. The components of $\mathbf{u}$ are denoted by $u_m(\mathbf{x},t)$, $m = 1,\ldots,n_d$. The stress tensor for an incompressible solid is

$$\underline{\underline{\boldsymbol{\sigma}}} = -pI + \mu\big(\nabla\mathbf{u} + (\nabla\mathbf{u})^T\big), \tag{2}$$

where $p = p(\mathbf{x},t)$ is the pressure and μ is a Lamé parameter, also taken here to be constant. These equations will be augmented with initial conditions for $\mathbf{u}$ and $\partial_t\mathbf{u}$ together with appropriate boundary conditions as discussed below. The system in (1) can be written in the equivalent form

$$\partial_t^2\mathbf{u} = -\frac{1}{\rho}\nabla p + c^2\Delta\mathbf{u}, \tag{3a}$$

$$\nabla\cdot\mathbf{u} = 0, \tag{3b}$$

where c is the shear wave speed,

$$c \stackrel{\text{def}}{=} \sqrt{\frac{\mu}{\rho}}. \tag{4}$$

Taking the divergence of (3a) and using (3b) gives a Poisson equation for the pressure and this leads to an alternative *displacement-pressure* form of the equations given by

$$\partial_t^2\mathbf{u} = -\frac{1}{\rho}\nabla p + c^2\Delta\mathbf{u}, \qquad \mathbf{x}\in\Omega, \quad t>0, \tag{5a}$$

$$\frac{1}{\rho}\Delta p = \frac{c_d}{\Delta t}\nabla\cdot(\partial_t\mathbf{u}), \qquad \mathbf{x}\in\Omega, \quad t>0. \tag{5b}$$

In (5) the divergence equation (3b) has been replaced by a Poisson equation for the pressure (5b), which also includes a divergence damping term as discussed below. Note that the displacement-pressure form requires an additional boundary condition which is taken to be $\nabla\cdot\mathbf{u} = 0$ for $\mathbf{x}\in\partial\Omega$. See [2, 3], for example, for a discussion of this boundary condition in the context of the incompressible Navier-Stokes equations, which is closely related to the present work.

The divergence damping term added to the right-hand side of (5b) uses a constant damping coefficient c_d with Δt denoting a time-step. This term is zero at the continuous level, but is useful in practical computations to keep the discrete divergence small. The action of the divergence damping term can be understood as follows. Taking the divergence of (5a) leads to a PDE for the divergence, $\delta = \nabla\cdot\mathbf{u}$,

$$\partial_t^2\delta = -\frac{1}{\rho}\Delta p + c^2\Delta\delta. \tag{6}$$

Substituting (5b) into (6) gives a damped wave equation for δ,

$$\partial_t^2\delta = -\frac{c_d}{\Delta t}\partial_t\delta + c^2\Delta\delta. \tag{7}$$

Thus, while formally zero at the continuous level, the term added to the right-hand-side of the pressure equation (5b) corresponds to a potentially large damping of any discretely generated spurious divergence. Also note that the solution of (7) together with the boundary condition $\delta = 0$ implies that $\delta(\mathbf{x},t)$ is identically zero throughout the domain. This explains why the additional boundary condition $\nabla\cdot\mathbf{u} = 0$ is used with the displacement-pressure formulation (5) since then

sufficiently smooth solutions to the displacement-pressure formulation will also be solutions to the displacement-divergence formulation[4].

An analysis of the energy in a system can be used to establish well-posedness of the system for suitable boundary conditions. Taking the L_2-inner product of (1) with $\partial_t \mathbf{u}$, over the domain Ω, results in

$$(\partial_t \mathbf{u}, \rho \partial_t^2 \mathbf{u})_\Omega = (\partial_t \mathbf{u}, \underline{\underline{\boldsymbol{\sigma}}})_\Omega. \tag{8}$$

Integration by parts gives

$$\frac{\rho}{2}\frac{d}{dt}\|\partial_t \mathbf{u}\|_\Omega^2 = (\partial_t \nabla \cdot \mathbf{u}, p)_\Omega - \frac{\mu}{2}\frac{d}{dt}\|\nabla \mathbf{u}\|_\Omega^2 + \int_{\partial\Omega} (\partial_t \mathbf{u})^T \underline{\underline{\boldsymbol{\sigma}}}\mathbf{n}\, dS, \tag{9}$$

where $\mathbf{n}$ is the outward unit normal to the boundary. Using $\nabla \cdot \mathbf{u} = 0$ leads to

$$\frac{d\mathcal{E}}{dt} = \int_{\partial\Omega} (\partial_t \mathbf{u})\, \underline{\underline{\boldsymbol{\sigma}}}\, \mathbf{n}\, dS, \tag{10}$$

which describes the evolution of the elastic energy, $\mathcal{E}(t)$, composed of kinetic and potential energies given by

$$\mathcal{E} \stackrel{\text{def}}{=} \frac{\rho}{2}\|\partial_t \mathbf{u}\|_\Omega^2 + \frac{\mu}{2}\|\nabla \mathbf{u}\|_\Omega^2. \tag{11}$$

Equation (10) indicates appropriate forms of well-posed boundary conditions with typical forms being a specification of $\mathbf{u}$ on a displacement boundary Γ_D,

$$\mathbf{u}(\mathbf{x}, t) = \mathbf{g}(\mathbf{x}, t), \qquad \mathbf{x} \in \Gamma_D, \tag{12}$$

or specifying the traction $\mathbf{t} = \underline{\underline{\boldsymbol{\sigma}}}\mathbf{n}$ on a traction boundary Γ_T,

$$\underline{\underline{\boldsymbol{\sigma}}}\mathbf{n} = \mathbf{g}(\mathbf{x}, t), \qquad \mathbf{x} \in \Gamma_T. \tag{13}$$

Other boundary conditions leading to a well-posed problem are also possible, such as periodic boundary conditions.

3. Fractional-step schemes, boundary conditions and upwind dissipation

In this section, two fractional-step schemes for the numerical solution of the displacement-pressure form (5) of the equations are described. In the first, the second-order form of the system in (5) is discretized directly in both space and time, leading to an efficient single-step fractional-step scheme. In the second, a method-of-lines formulation for the equations written as a first-order system in time but second-order in space is considered. In the present work, a scheme based on an Adams predictor-corrector time integrator is proposed. Other time-integrators could be used, such as Runge-Kutta (RK) schemes, provided they are stable on the imaginary axis (such as the traditional RK4 scheme). After presenting the two basic schemes, the discretization of the boundary conditions is discussed. Finally a method of upwind dissipation is presented, which is included in the time-stepping schemes. This section ends with a discussion of the choice of a stable time-step.

[4]Note that other additional boundary conditions could be used, such as a Robin condition on δ.

3.1. Second-order accurate fractional-step scheme for the SOS formulation

The second-order system, modified equation (SOS-ME) scheme is now described. It is a second-order accurate fractional-step scheme that solves the displacement-pressure equations (5) in second-order form in both time and space. Let $\mathbf{x_i} \in \mathbb{R}^{n_d}$ denote the grid points on a structured grid, where $\mathbf{i} = [i_1, \ldots, i_{n_d}] \in \mathbb{Z}^{n_d}$ is a multi-index of integer components. Let $\mathbf{u}_\mathbf{i}^n \approx u(\mathbf{x_i}, t^n)$ and $p_\mathbf{i}^n \approx p(\mathbf{x_i}, t^n)$ denote discrete approximations to the displacement and pressure, respectively, at time $t^n = n\Delta t$, where Δt is the time-step. Let D_{+t}, D_{-t}, D_{0t} denote the standard divided difference operators in time, defined by

$$D_{+t}\mathbf{u}_\mathbf{i}^n \stackrel{\text{def}}{=} \frac{\mathbf{u}_\mathbf{i}^{n+1} - \mathbf{u}_\mathbf{i}^n}{\Delta t}, \qquad D_{-t}\mathbf{u}_\mathbf{i}^n \stackrel{\text{def}}{=} \frac{\mathbf{u}_\mathbf{i}^n - \mathbf{u}_\mathbf{i}^{n-1}}{\Delta t}, \qquad D_{0t}\mathbf{u}_\mathbf{i}^n \stackrel{\text{def}}{=} \frac{\mathbf{u}_\mathbf{i}^{n+1} - \mathbf{u}_\mathbf{i}^{n-1}}{2\Delta t}. \tag{14}$$

Similarly the undivided difference operators are defined

$$\Delta_{+t}\mathbf{u}_\mathbf{i}^n \stackrel{\text{def}}{=} \mathbf{u}_\mathbf{i}^{n+1} - \mathbf{u}_\mathbf{i}^n, \qquad \Delta_{-t}\mathbf{u}_\mathbf{i}^n \stackrel{\text{def}}{=} \mathbf{u}_\mathbf{i}^n - \mathbf{u}_\mathbf{i}^{n-1}, \qquad \Delta_{0t}\mathbf{u}_\mathbf{i}^n \stackrel{\text{def}}{=} \mathbf{u}_\mathbf{i}^{n+1} - \mathbf{u}_\mathbf{i}^{n-1}. \tag{15}$$

Algorithm 1 Second-order accurate SOS-ME-fractional-step scheme.

function advanceSOS
  // Assign initial conditions.
  $t = 0, \quad n = 0.$
  while $t \le t_{\text{final}}$ **do** ▷ Begin time-stepping loop
    $\dfrac{\mathbf{u}_\mathbf{i}^p - 2\mathbf{u}_\mathbf{i}^n + \mathbf{u}_\mathbf{i}^{n-1}}{\Delta t^2} = -\dfrac{1}{\rho}\nabla_h p_\mathbf{i}^n + c^2\Delta_h \mathbf{u}_\mathbf{i}^n\ , \qquad \mathbf{i} \in \Omega_h,$
    $\mathbf{u}^p =$ applyBoundaryConditions($\mathbf{u}^p$, $t + \Delta t$) ,
    $\mathbf{u}^{n+1} =$ addUpwindDissipation($\mathbf{u}^p$, $\mathbf{u}^{n-1}$, $t + \Delta t$) ,
    $p^{n+1} =$ solveForPressure($\mathbf{u}^{n+1}$, $\mathbf{u}^n$),
    $t = t + \Delta t, \quad n = n + 1.$
  end while ▷ End time-stepping loop
end function

function $\mathbf{u}^{n+1} =$ addUpwindDissipation($\mathbf{u}^p$, $\mathbf{u}^{n-1}$, t)
  $\mathbf{u}_\mathbf{i}^{n+1} = \mathbf{u}_\mathbf{i}^p - \Delta t^2 \beta_4 \sum_{m=1}^{n_d} \dfrac{c\,\|\nabla_h r_m\|}{\Delta r_m}\big(\Delta_{+r_m}\Delta_{-r_m}\big)^2\Big(\dfrac{\mathbf{u}_\mathbf{i}^p - \mathbf{u}_\mathbf{i}^{n-1}}{2\Delta t}\Big), \qquad \mathbf{i} \in \Omega_h,$
  $\mathbf{u}^{n+1} =$ applyBoundaryConditions($\mathbf{u}^{n+1}$, t) .
end function

function $p^{n+1} =$ solveForPressure($\mathbf{u}^{n+1}$, $\mathbf{u}^n$)
  // Solve the Poisson equation.
  $\Delta_h p_\mathbf{i}^{n+1} = \rho\,\dfrac{c_d}{\Delta t}\nabla_h \cdot (\mathbf{u}^{n+1} - \mathbf{u}^n)/\Delta t, \qquad \mathbf{i} \in \Omega_{h,P},$
  $\mathbf{n_i} \cdot \nabla_h p_\mathbf{i}^{n+1} = \mu\,(\mathbf{n_i})^T \Delta_h \mathbf{u}_\mathbf{i}^{n+1}, \qquad \mathbf{i} \in \Gamma_{h,D},$
  $p_\mathbf{i}^{n+1} = 2\mu(\mathbf{n_i})^T\big((\mathbf{n_i} \cdot \nabla_h)\mathbf{u}_\mathbf{i}^{n+1}\big), \qquad \mathbf{i} \in \Gamma_{h,T}.$
end function

Each time-step of the SOS-ME scheme involves two stages. In the first stage, the displacement is advanced in time using a second-order accurate centered approximation to the momentum equation (3a) given by

$$D_{+t}D_{-t}\mathbf{u}_\mathbf{i}^n = -\frac{1}{\rho}\nabla_h p_\mathbf{i}^n + c^2\Delta_h \mathbf{u}_\mathbf{i}^n, \tag{16}$$

where ∇_h and Δ_h denote second-order accurate centered difference approximations of the spatial operators ∇ and Δ, respectively. Approximations to ∇_h and Δ_h for Cartesian grids and logically rectangular curvilinear grids are given in Section 5, as well as a discussion of the application of overlapping grids to handle complex domains. The first stage ends with discrete boundary conditions applied to $\mathbf{u}_{\mathbf{i}}^{n+1}$ as discussed in Section 3.3. In the second stage of the SOS-ME scheme, the pressure is computed by solving the discrete Poisson equation

$$\frac{1}{\rho}\Delta_h p_{\mathbf{i}}^{n+1} = \frac{c_d}{\Delta t}\nabla_h \cdot \left(D_{-t}\mathbf{u}_{\mathbf{i}}^{n+1}\right), \tag{17}$$

using appropriate boundary conditions on $p_{\mathbf{i}}^{n+1}$, which are also discussed in Section 3.3.

The fractional-step scheme is summarized in the Algorithm 1. The algorithm also includes upwind dissipation which is discussed in Section 3.4.

Algorithm 2 Second-order accurate FOT-PC-fractional-step predictor-corrector scheme

function advancePredictorCorrector
  // Assign initial conditions.
  $t = 0, \quad n = 0.$
  while $t \le t_{\text{final}}$ **do** ▷ Begin time-stepping loop
    // Predictor stage.
    $[\dot{\mathbf{u}}^n, \dot{\mathbf{v}}^n] =$ getUt($\mathbf{u}^n, \mathbf{v}^n, p^n$) ,
    $\begin{bmatrix}\mathbf{u}^p \\ \mathbf{v}^p\end{bmatrix} = \begin{bmatrix}\mathbf{u}^n \\ \mathbf{v}^n\end{bmatrix} + \frac{3\Delta t}{2}\begin{bmatrix}\dot{\mathbf{u}}^n \\ \dot{\mathbf{v}}^n\end{bmatrix} - \frac{\Delta t}{2}\begin{bmatrix}\dot{\mathbf{u}}^{n-1} \\ \dot{\mathbf{v}}^{n-1}\end{bmatrix}$, ▷ Adams-Bashforth predictor
    $\mathbf{u}^p =$ applyBoundaryConditions($\mathbf{u}^p, t + \Delta t$) ,
    $\mathbf{u}^p =$ addUpwindDissipation($\mathbf{u}^p, \mathbf{u}^{n-1}, t + \Delta t$) ,
    $p^p =$ solveForPressure($\mathbf{u}^p, \mathbf{u}^n$),
    // Corrector stage.
    $[\dot{\mathbf{u}}^p, \dot{\mathbf{v}}^p] =$ getUt($\mathbf{u}^p, \mathbf{v}^p, p^p$) ,
    $\begin{bmatrix}\mathbf{u}^{n+1} \\ \mathbf{v}^{n+1}\end{bmatrix} = \begin{bmatrix}\mathbf{u}^n \\ \mathbf{v}^n\end{bmatrix} + \frac{\Delta t}{2}\begin{bmatrix}\dot{\mathbf{u}}^p \\ \dot{\mathbf{v}}^p\end{bmatrix} + \frac{\Delta t}{2}\begin{bmatrix}\dot{\mathbf{u}}^n \\ \dot{\mathbf{v}}^n\end{bmatrix}$, ▷ Adams-Moulton (trapezoidal rule) corrector
    $\mathbf{u}^{n+1} =$ applyBoundaryConditions($\mathbf{u}^{n+1}, t + \Delta t$) ,
    $\mathbf{u}^{n+1} =$ addUpwindDissipation($\mathbf{u}^{n+1}, \mathbf{u}^{n-1}, t + \Delta t$) ,
    $p^{n+1} =$ solveForPressure($\mathbf{u}^{n+1}, \mathbf{u}^n$),
    $t = t + \Delta t, \quad n = n + 1.$
  end while ▷ End time-stepping loop
end function

function $[\dot{\mathbf{u}}, \dot{\mathbf{v}}]$ = getUt($\mathbf{u}, \mathbf{v}, p$)
  $\dot{\mathbf{u}}_{\mathbf{i}} = \mathbf{v}_{\mathbf{i}}$, $\quad \mathbf{i} \in \Omega_h,$
  $\dot{\mathbf{v}}_{\mathbf{i}} = -\frac{1}{\rho}\nabla_h p_{\mathbf{i}} + c^2\Delta_h \mathbf{u}_{\mathbf{i}}, \quad \mathbf{i} \in \Omega_h.$
end function

3.2. Fractional-step predictor-corrector scheme for the FOT formulation

In this section we describe the FOT-PC scheme which employs a predictor-corrector time-stepping scheme for the system in (5) expressed as a first-order system in time. The development of this scheme is partially motivated by our Added-Mass Partitioned (AMP) schemes for fluid-structure interaction problems which often make use of predictor-corrector schemes which incorporate discrete approximations of the solid velocity and traction at an interface [17–24]. The governing equations can be written as a first-order system in time by introducing the velocity $\mathbf{v} = \partial_t \mathbf{u}$, leading

to

$$\partial_t \mathbf{u} = \mathbf{v}, \qquad \mathbf{x} \in \Omega, \quad t > 0, \tag{18a}$$

$$\partial_t \mathbf{v} = -\frac{1}{\rho}\nabla p + \frac{\mu}{\rho}\Delta \mathbf{u}, \qquad \mathbf{x} \in \Omega, \quad t > 0, \tag{18b}$$

$$\frac{1}{\rho}\Delta p = \frac{c_d}{\Delta t}\,\nabla \cdot \mathbf{v}, \qquad \mathbf{x} \in \Omega, \quad t > 0. \tag{18c}$$

The FOT formulation in (18) can be discretized using a method-of-lines (MOL) approach involving a linear multi-step method or a Runge-Kutta scheme, for example. Here we illustrate the fractional-step MOL approach using a multi-step predictor-corrector scheme consisting of a second-order accurate Adams-Bashforth predictor and a second-order accurate Adams-Moulton (trapezoidal rule) corrector. The FOT-PC scheme is summarized in Algorithm 2. The steps in the predictor and corrector stages are similar. In the first step, discrete approximations for the displacement and velocity are advanced in time leading to predicted values at t^{n+1} denoted by $\mathbf{u}^p$ and $\mathbf{v}^p$. The subsequent steps involve an application of boundary conditions and an upwind dissipation using similar functions calls to those in the SOS-ME scheme. The final step of the predictor stage involves a solution of a discrete Poisson problem to compute the predicted pressure denoted by p^p. The set of steps in the corrector stage, following those of the predictor stage, lead to the calculation of the displacement, velocity and pressure at t^{n+1}.

3.3. Discrete approximations to the boundary conditions.

Careful attention to the discrete boundary conditions is important in order to retain second-order accuracy for the fractional-step scheme and to ensure stability, especially in the case of traction boundary conditions. In this section we give a brief description of the equations used to discretize the boundary conditions, including the use of compatibility boundary conditions (CBCs) where appropriate. As discussed in more detail in Section 5, we discretize the interior scheme and boundary conditions on a structured grid. The grid points are denoted by $\mathbf{x}_\mathbf{i}$, where $\mathbf{i} = [i_1, i_2, i_3]$ is a multi-index. The grid-point indicies for the interior and boundary points are given by $i_m = 0, 1, 2, \ldots, N_m$, where N_m is the number of grid cells in direction m, $m = 0, 1, \ldots, n_d$. Ghost points are added outside this primary grid as shown in Figure 2. Given the index $\mathbf{i}$ of a point on the boundary (e.g. $\mathbf{i} = [0, i_2, i_3]$ for a point on the left boundary), the adjacent ghost point is denoted by $\mathbf{j}$ (e.g. $\mathbf{j} = [-1, i_2, i_3]$). The stencil for a typical discrete boundary condition that involves first derivatives is also shown in Figure 2.

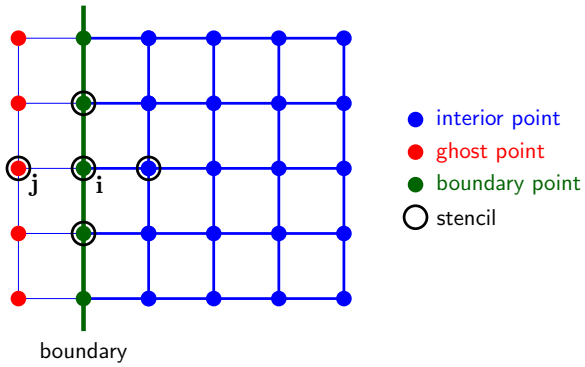

Figure 2: Grid points near a left boundary showing interior, boundary and ghost points. The stencil for a typical discrete boundary condition that involves first derivatives is also shown.

Displacement boundary conditions. The discrete boundary conditions for $\mathbf{u}$ on a displacement boundary are

$$\mathbf{u}_{\mathbf{i}}^n = \mathbf{g}(\mathbf{x}_{\mathbf{i}}, t^n), \qquad \mathbf{i} \in \Gamma_{h,D}, \tag{19a}$$

$$\nabla_h \cdot \mathbf{u}_{\mathbf{i}}^n = 0, \qquad \mathbf{i} \in \Gamma_{h,D}, \tag{19b}$$

$$\text{Extrapolate}((\mathbf{t}_{m,\mathbf{i}})^T \mathbf{u}_{\mathbf{j}}^n), \qquad \mathbf{i} \in \Gamma_{h,D}, \tag{19c}$$

where $\mathbf{j}$ denotes the index of ghost point adjacent to the boundary point with index $\mathbf{i}$, $\Gamma_{h,D}$ denotes the set of points on the displacement boundary, and $\mathbf{t}_{m,\mathbf{i}}$, $m = 1, \ldots, n_d - 1$, are linearly independent tangent vectors on the boundary (see Figure 2). Here, (19a) is the primary displacement boundary condition, while (19b) sets the divergence on the boundary to be zero as required in the pressure Poisson formulation. The last condition in (19c) is a numerical boundary condition that extrapolates the tangential components of $\mathbf{u}$ to the ghost points. Consider, for example, a ghost point on the left boundary in parameter space, $\mathbf{u}_{\mathbf{j}} \stackrel{\text{def}}{=} \mathbf{u}_{i_1-1,i_2,i_3}$. We use three-point extrapolation, which derives from the condition[5] $\mathbf{t}_{m,\mathbf{i}}^T D_{+r_1}^3 \mathbf{u}_{\mathbf{j}}^n = 0$, and this leads to the formula

$$\mathbf{t}_{m,\mathbf{i}}^T \mathbf{u}_{\mathbf{j}} \stackrel{\text{def}}{=} \mathbf{t}_{m,\mathbf{i}}^T \mathbf{u}_{\mathbf{i}-\mathbf{e}_1} = \mathbf{t}_{m,\mathbf{i}}^T \big(3\mathbf{u}_{\mathbf{i}} - 3\mathbf{u}_{\mathbf{i}+\mathbf{e}_1} + \mathbf{u}_{\mathbf{i}+2\mathbf{e}_1}\big). \tag{20}$$

Equations (19b) and (20) then define n_d linear equations for the n_d ghost point values in $\mathbf{u}_{\mathbf{j}}$ which can be expressed as

$$M_D \mathbf{u}_{\mathbf{j}}^n = \mathbf{r}_D, \tag{21}$$

for a matrix $M_D \in \mathbb{R}^{n_d \times n_d}$, and for a right-hand side vector $\mathbf{r}_D$ which depends on solution values from the interior and boundary. The linear system in (21) is then solved for $\mathbf{u}_{\mathbf{j}}^n$. Note that on a Cartesian grid, or an orthogonal grid, the tangential component of $\mathbf{u}$ on the ghost point is not used in any other equations and thus using extrapolation does not appear to adversely effect stability, even though extrapolation (and one-sided approximations) should often be avoided from a stability perspective[6]. The boundary condition for the pressure on a displacement boundary is

$$\mathbf{n}_{\mathbf{i}} \cdot \nabla_h p_{\mathbf{i}}^n = (\mathbf{n}_{\mathbf{i}})^T (\mu \, \Delta_h \mathbf{u}_{\mathbf{i}}^n), \qquad \mathbf{i} \in \Gamma_{h,D}. \tag{22}$$

Equation (22) is called a compatibility boundary condition (CBC) since it is not a true physical boundary condition but rather the interior equation applied on the boundary. In this regard, condition (19b), imposing the divergence of the displacement to be zero on the boundary, can also be viewed as a CBC.

Traction boundary conditions. At the continuous level, the traction boundary conditions, $\boldsymbol{\sigma}\mathbf{n} = 0$, with $\nabla \cdot \mathbf{u} = 0$, lead to

$$p = 2\mu \, \mathbf{n}^T (\partial_{\mathbf{n}} \mathbf{u}), \qquad \mathbf{x} \in \Gamma_T, \tag{23a}$$

$$\mathbf{t}_m^T \underline{\boldsymbol{\sigma}} \, \mathbf{n} = 0, \qquad \mathbf{x} \in \Gamma_T, \quad m = 1, \ldots, n_d - 1, \tag{23b}$$

$$\nabla \cdot \mathbf{u} = 0, \qquad \mathbf{x} \in \Gamma_T, \tag{23c}$$

where (23a) comes from $\mathbf{n}^T \boldsymbol{\sigma} \mathbf{n} = 0$ and the definition of $\boldsymbol{\sigma}$ in (2). (We have assumed homogeneous conditions for clarity.) Equation (23a) is used as a boundary condition for the pressure when

[5] D_{+r_1} is the forward difference operator in parameter space as defined in (90).

[6] Finite-Difference Golden Rule No. 3: Avoid extrapolation as it amplifies high-frequency errors [28].

solving the pressure Poisson equation, while (23b) and (23c) are used as boundary conditions for the displacement. The discrete boundary conditions in (23b) and (23c) for the displacement $\mathbf{u}$ on a traction boundary can be written compactly as

$$(\nabla_h \cdot \mathbf{u}_\mathbf{i}^n)\,\mathbf{n}_\mathbf{i} + (I - \mathbf{n}_\mathbf{i}(\mathbf{n}_\mathbf{i})^T)\,\mu\left(\nabla_h \mathbf{u}_\mathbf{i}^n + (\nabla_h \mathbf{u}_\mathbf{i}^n)^T\right)\mathbf{n}_\mathbf{i} = 0, \qquad \mathbf{i} \in \Gamma_{h,T}, \tag{24}$$

where $\Gamma_{h,T}$ denotes the set of points on the traction boundary. To see why this is so, note that taking the dot-product of the normal vector $\mathbf{n}_\mathbf{i}$ with (24) gives the discrete version of the divergence boundary condition (23c). Taking the dot-product of a tangent vector $\mathbf{t}_m$ with (24) gives the discrete version of (23b). The formulation (24) is advantageous since it is defined just in terms of the normal vector and does not require forming the tangent vectors [22]. Note that on a traction boundary, the interior equations in (16) are updated on the boundary and the conditions in (24) are used to fill in ghost values. In particular, when discretized, equations (24) can be written as a small matrix system for the unknown ghost values in $\mathbf{u}_\mathbf{j}^n$,

$$M_N \mathbf{u}_\mathbf{j}^n = \mathbf{r}_N, \tag{25}$$

for a matrix $M_N \in \mathbb{R}^{n_d \times n_d}$, and for a right-hand-side vector $\mathbf{r}_N$ which depends on solution values from the interior and boundary. The system in (25) is then solved for ghost values $\mathbf{u}_\mathbf{j}^n$.

The discrete boundary conditions for the pressure on a traction boundary are

$$p_\mathbf{i}^n = 2\mu(\mathbf{n}_\mathbf{i})^T\big((\mathbf{n}_\mathbf{i} \cdot \nabla_h)\mathbf{u}_\mathbf{i}^n\big), \qquad \mathbf{i} \in \Gamma_{h,T}, \tag{26a}$$

$$\Delta_h\, p_\mathbf{i}^n = 0, \qquad \mathbf{i} \in \Gamma_{h,T}. \tag{26b}$$

Note that (26a) is a discretization of $\mathbf{n}^T \underline{\underline{\boldsymbol{\sigma}}} \mathbf{n} = 0$ on the boundary, and that (26b) is a compatibility condition (recall that (24) sets the discrete divergence to zero on the boundary and so the divergence damping term vanishes). On a traction boundary, CBCs are also employed. First of all, the interior equations for the displacement are applied on the boundary itself. These displacement equations require values of the pressure on the first ghost point and these pressure values are obtained in a centered manner by applying the interior pressure equation on the boundary using (26b). Equation (26b) can be viewed as an equation for the pressure in the set of ghost points immediately adjacent to the boundary.

To clarify the meaning of these discrete boundary conditions in a simple setting, consider a Cartesian grid in three dimensions with boundary at $x_1 = 0$. Using the usual divided difference operators $D_{\pm x_m}$ and D_{0x_m} as defined in Section 5, the traction conditions for the displacement (24) simplify to

$$D_{0x_1} u_{2,\mathbf{i}}^n + D_{0x_2} u_{1,\mathbf{i}}^n = 0, \qquad \mathbf{i} \in \Gamma_{h,T}, \tag{27a}$$

$$D_{0x_1} u_{3,\mathbf{i}}^n + D_{0x_3} u_{1,\mathbf{i}}^n = 0, \qquad \mathbf{i} \in \Gamma_{h,T}, \tag{27b}$$

$$D_{0x_1} u_{1,\mathbf{i}}^n + D_{0x_2} u_{2,\mathbf{i}}^n + D_{0x_3} u_{3,\mathbf{i}}^n = 0, \qquad \mathbf{i} \in \Gamma_{h,T}. \tag{27c}$$

Here (27c) is a discrete version of the divergence boundary condition (23c), while (27a) and (27b) are discrete versions of the pair of the primal traction conditions in (23b). For example, when explicitly written out, condition (27a) is

$$\frac{u_{2,i_1+1,i_2,i_3}^n - u_{2,i_1-1,i_2,i_3}^n}{2\Delta x_1} + \frac{u_{1,i_1,i_2+1,i_3}^n - u_{1,i_1,i_2-1,i_3}^n}{2\Delta x_2} = 0, \tag{28}$$

where Δx_m denotes the grid spacing in direction m. Solving (28) for u^n_{2,i_1-1,i_2,i_3} gives the following update for the value of $u_{2,\mathbf{i}}$ at the first ghost point,

$$u^n_{2,i_1-1,i_2,i_3} = u^n_{2,i_1+1,i_2,i_3} + (2\Delta x_1)\frac{u^n_{1,i_1,i_2+1,i_3} - u^n_{1,i_1,i_2-1,i_3}}{2\Delta x_2}. \tag{29}$$

Similarly, the discrete pressure boundary conditions (26) in a Cartesian grid setting are

$$p^n_{\mathbf{i}} = 2\mu\, D_{0x_1} u^n_{1,\mathbf{i}}, \qquad \mathbf{i} \in \Gamma_{h,T}, \tag{30a}$$

$$\left(D_{+x_1}D_{-x_1} + D_{+x_2}D_{-x_2} + D_{+x_3}D_{-x_3}\right) p^n_{\mathbf{i}} = 0, \qquad \mathbf{i} \in \Gamma_{h,T}. \tag{30b}$$

3.4. Upwind dissipation

Upwind dissipation is added to stabilize the scheme. The governing equations have no natural dissipation, and thus discrete schemes are susceptible to numerical instabilities. Schemes for wave equations on overset grids typically require some dissipation to avoid instabilities [26, 27, 29–31]. In addition, finite difference schemes for elasticity are known to have difficulty at traction boundaries even on a single Cartesian grid [5]. Upwind dissipation has been found to be stabilizing in both of these scenarios, and here we adopt an optimized upwind formulation developed for wave equations in [25–27]. At a continuous level the upwind dissipation takes the form of a hyper-dissipation

$$\partial_t^2 \mathbf{u} = -\frac{1}{\rho}\nabla p + c^2 \Delta \mathbf{u} - c\beta_4 \sum_{m=1}^{n_d} \Delta x_m^3 \partial_{x_m}^4 \partial_t \mathbf{u}, \tag{31}$$

where Δx_m represents the grid spacing in the x_m coordinate direction, and where β_4 is a coefficient (given below). Note that formally the upwind dissipation in (31) represents an $\mathcal{O}(h^3)$ correction and thus does not affect the accuracy of the scheme. To avoid a time-step restriction, the dissipation is added to the scheme (16) in a predictor-corrector (operator split) fashion as shown in Algorithm 1. The predictor step is

$$\frac{\mathbf{u}^p_{\mathbf{i}} - 2\mathbf{u}^n_{\mathbf{i}} + \mathbf{u}^{n-1}_{\mathbf{i}}}{\Delta t^2} = -\frac{1}{\rho}\nabla_h p^n_{\mathbf{i}} + c^2 \Delta_h \mathbf{u}^n_{\mathbf{i}}. \tag{32}$$

The upwind-dissipation corrector-step on a Cartesian grid[7] is

$$\mathbf{u}^{n+1}_{\mathbf{i}} = \mathbf{u}^p_{\mathbf{i}} - \Delta t^2 \beta_4 \sum_{m=1}^{n_d} \frac{c}{\Delta x_m}\left(\Delta_{+x_m}\Delta_{-x_m}\right)^2 \left(\frac{\mathbf{u}^p_{\mathbf{i}} - \mathbf{u}^{n-1}_{\mathbf{i}}}{2\Delta t}\right), \tag{33}$$

where β_4 is chosen to be

$$\beta_4 = \frac{1}{8\sqrt{n_d}}. \tag{34}$$

Here Δ_{+x_m} and Δ_{-x_m} are the usual undivided difference approximations. With this value of β_4, obtained from a von Neumann stability analysis, the time-step restriction for the scheme remains the same as with no dissipation. Larger values of β_4 would require reductions in the time-step [27]. Note that the upwind dissipation operator uses a wider five-point stencil in each direction. This requires an additional ghost line to be assigned on traction boundaries (but not displacement boundaries).

[7] The form of the upwinding for curvilinear grids is given by (96) in Section 5.

The wider stencil is a key component of the upwinding and arises from the wave equation having waves that propagate in both directions, as opposed to first-order hyperbolic systems where the upwinding is biased in the upwind direction for each characteristic variable.

As noted above, upwinding, when used with traction boundaries, requires values for the displacement on an additional ghost line. These extra values are obtained by using similar discrete approximations used to obtain the first ghost point, but using formulae based on a grid with twice the grid spacings in each direction.

4. Stability of the fractional-step scheme

The stability of the new schemes is now investigated. Section 4.1 presents a von Neumann analysis to derive a time-step restriction for each scheme, including the effects of the divergence damping. This is followed in Section 4.2 by a GKS stability analysis of a model problem to assess the stability of the SOS-ME scheme with traction and displacement boundary conditions. This analysis shows the necessity of including upwind dissipation for problems with traction boundary conditions.

4.1. Time-step determination and divergence damping

We begin with a derivation of the time-step restrictions for the schemes. We determine the maximal stable time-step using von Neumann analysis and also determine bounds on the divergence damping coefficient, c_d, so that the damping term does not force a reduction in the time-step. We find that the maximal time-step follows the usual formula for a scalar wave equation provided the divergence damping coefficient lies in the range $0 \leq c_d < 2$.

First, consider the SOS-ME scheme given by

$$D_{+t}D_{-t}\mathbf{u}_{\mathbf{i}}^n + \frac{1}{\rho}\nabla_h p_{\mathbf{i}}^n = c^2\Delta_h \mathbf{u}_{\mathbf{i}}^n, \tag{35a}$$

$$\frac{1}{\rho}\Delta_h p_{\mathbf{i}}^n = \frac{c_d}{\Delta t}\nabla_h \cdot \left(D_{-t}\mathbf{u}_{\mathbf{i}}^n\right), \tag{35b}$$

using second-order accurate spatial approximations on a Cartesian grid covering $\Omega = [0, 2\pi]^{n_d}$. The time-step restriction for the time-stepping scheme is given in the Theorem 1 assuming periodic boundaries in all directions. The proof employs a von Neumann analysis and is given in Appendix A.

Theorem 1 (Time-step restriction and divergence damping)**.** *The time-step restriction for the SOS-ME scheme (35) on a Cartesian grid with periodic boundary conditions is*

$$\lambda_{\text{CFL}}^2 \stackrel{\text{def}}{=} c^2\,\Delta t^2 \left(\sum_{m=1}^{n_d} \frac{1}{\Delta x_m^2}\right) < 1, \tag{36}$$

provided the coefficient of divergence damping satisfies

$$0 \leq c_d < 2. \tag{37}$$

Following a similar von Neumann analysis of a method-of-lines (MOL) approximation, the time-step restriction for the FOT-PC scheme on a Cartesian grid is estimated to be

$$\lambda_{\text{CFL}} < \frac{1}{2}\, b_{\text{MOL}} \approx 0.65 \tag{38}$$

where $b_{\text{MOL}} \approx 1.3$ is a bound on the positive imaginary axis of the region of absolute stability of the Adams predictor-corrector scheme applied to the test equation, $y' = \lambda y$. For reference, the RK4 stability bound is $b_{\text{MOL}} \approx 2.8$.

The SOS-ME scheme is thus seen to be significantly more efficient than the FOT-PC scheme. The former allows a larger stable time-step and requires only one update for the displacement and pressure per global step, while the latter needs two updates for the displacement, velocity, and pressure per global step.

4.2. GKS stability analysis of a half-plane problem

In view of the fact that many traditional finite difference schemes for compressible elasticity with traction boundaries are known to be unstable in the incompressible limit [5], it is natural to ask if the schemes proposed here are stable for problems with traction boundaries. To address this question, we study a model half-plane problem in two space dimensions using classical GKS stability theory for initial-boundary-value problems [32, 33]. We investigate the stability of the SOS-ME scheme. To clarify the exposition and simplify the analysis, we omit the divergence damping term in the pressure-Poisson problem and utilize a first-order accurate upwind dissipation. Neither of these simplifications result in a material change to the central conclusions (e.g. that for traction boundaries the centered scheme is unstable while upwind schemes are stable), and the relevance of the analysis to the full scheme is made clear by the results presented in Section 6. We first show that the scheme is stable (has no exponentially growing modes) with displacement boundary conditions. We then investigate the more difficult case of traction boundary conditions and show the scheme without upwind dissipation is unstable, while the addition of upwind dissipation stabilizes the method.

Consider the following discrete approximation for the equations of incompressible linear elasticity in displacement-pressure form using a first-order accurate upwind dissipation,

$$D_{+t}D_{-t}u^n_{1,\mathbf{i}} = c^2\Delta_h\, u^n_{1,\mathbf{i}} - \frac{1}{\rho}D_{0x}p^n_{\mathbf{i}} + c\beta(\Delta x D_{+x}D_{-x} + \Delta y D_{+y}D_{-y})D_{-t}u^n_{1,\mathbf{i}}, \tag{39a}$$

$$D_{+t}D_{-t}u^n_{2,\mathbf{i}} = c^2\Delta_h\, u^n_{2,\mathbf{i}} - \frac{1}{\rho}D_{0y}p^n_{\mathbf{i}} + c\beta(\Delta x D_{+x}D_{-x} + \Delta y D_{+y}D_{-y})D_{-t}u^n_{2,\mathbf{i}}, \tag{39b}$$

$$\Delta_h\, p^n_{\mathbf{i}} = 0, \tag{39c}$$

where β is the dissipation coefficient and the difference operators are defined in Section 5. Note that to clarify the exposition, we have adopted (x, y) to denote the spatial coordinates rather than (x_1, x_2). These equations are augmented by appropriate initial and boundary conditions.

Before performing a GKS analysis for the problem with physical boundaries, we first determine the stability condition for the initial-value problem with periodic boundary conditions. The result is given in the following theorem which is proved in Appendix B.

Theorem 2 (Stability of the periodic IVP)**.** *The discrete scheme* (39) *is stable with periodic boundary conditions provided*

$$(c\Delta t)^2\left(\frac{1}{\Delta x^2} + \frac{1}{\Delta y^2}\right) + 2\beta(c\Delta t)\left(\frac{1}{\Delta x} + \frac{1}{\Delta y}\right) \le 1. \tag{40}$$

Note that (40) imposes the following bound on β,

$$\beta(c\Delta t)\left(\frac{1}{\Delta x} + \frac{1}{\Delta y}\right) < \frac{1}{2}. \tag{41}$$

We now study the half-plane problem for $x > 0$ assuming periodic boundaries in the y direction. Performing a discrete Fourier transform in the y direction on the scheme in (39) gives

$$D_{+t}D_{-t}u^n_{1,j} = c^2(D_{+x}D_{-x} + \widehat{D_{yy}})u^n_{1,j} - \frac{1}{\rho}D_{0x}p^n_j + c\,\beta(\Delta x D_{+x}D_{-x} + \Delta y\widehat{D_{yy}})D_{-t}u^n_{1,j}, \tag{42a}$$

$$D_{+t}D_{-t}u^n_{2,j} = c^2(D_{+x}D_{-x} + \widehat{D_{yy}})u^n_{2,j} - \frac{1}{\rho}\widehat{D_y}p^n_j + c\,\beta(\Delta x D_{+x}D_{-x} + \Delta y\widehat{D_{yy}})D_{-t}u^n_{2,j}, \tag{42b}$$

$$(D_{+x}D_{-x} + \widehat{D_{yy}})p^n_j = 0, \tag{42c}$$

where grid functions such as $u^n_{1,j}$ are interpreted as the coefficient of the discrete Fourier transform in y with corresponding wave number k_y, and whose dependence is suppressed. Note that the difference operators in the y direction have reduced to the Fourier symbols

$$\widehat{D_y} \stackrel{\text{def}}{=} \frac{i\sin(\xi)}{\Delta y}, \qquad \widehat{D_{yy}} \stackrel{\text{def}}{=} \frac{2\cos(\xi) - 2}{\Delta y^2} = \frac{-4\sin^2(\xi/2)}{\Delta y^2}, \tag{43}$$

where $\xi = k_y\Delta y \in [-\pi, \pi]$.

In order to more clearly identify the relevant dimensionless parameters, it is useful to scale the equations in (42) to obtain

$$\delta_{+t}\delta_{-t}u^n_{1,j} = (\lambda_x^2\,\delta_{+x}\delta_{-x} + \lambda_y^2\,\widehat{\delta_{yy}})u^n_{1,j} - \lambda_x\,\delta_{0x}\tilde{p}^n_j + \beta(\lambda_x\,\delta_{+x}\delta_{-x} + \lambda_y\,\widehat{\delta_{yy}})\delta_{-t}u^n_{1,j}, \tag{44a}$$

$$\delta_{+t}\delta_{-t}u^n_{2,j} = (\lambda_x^2\,\delta_{+x}\delta_{-x} + \lambda_y^2\,\widehat{\delta_{yy}})u^n_{2,j} - \lambda_y\,\widehat{\delta_y}\tilde{p}^n_j + \beta(\lambda_x\,\delta_{+x}\delta_{-x} + \lambda_y\,\widehat{\delta_{yy}})\delta_{-t}u^n_{2,j}, \tag{44b}$$

$$(\delta_{+x}\delta_{-x} + \mathcal{R}^2\,\widehat{\delta_{yy}})\tilde{p}^n_j = 0, \tag{44c}$$

where δ is used to denote *undivided* difference operators and scaled Fourier symbols (e.g. $\delta_{+x} = \Delta x D_{+x}$, $\widehat{\delta_{yy}} = \Delta y^2\widehat{D_{yy}}$, etc.), and where

$$\tilde{u}^n_{1,j} = \frac{1}{l_0}u^n_{1,j}, \qquad \tilde{u}^n_{2,j} = \frac{1}{l_0}u^n_{2,j}, \qquad \tilde{p}^n_j \stackrel{\text{def}}{=} \frac{1}{\rho c(l_0/\Delta t)}p^n_j, \tag{45a}$$

$$\lambda_x \stackrel{\text{def}}{=} \frac{c\Delta t}{\Delta x}, \qquad \lambda_y \stackrel{\text{def}}{=} \frac{c\Delta t}{\Delta y}, \qquad \mathcal{R} \stackrel{\text{def}}{=} \frac{\Delta x}{\Delta y} = \frac{\lambda_y}{\lambda_x}, \tag{45b}$$

are dimensionless grid functions and parameters (using l_0 as some length scale for both components of displacement). Note that only two of the three parameters $(\lambda_x, \lambda_y, \mathcal{R})$ are independent since, for example, $\mathcal{R} = \lambda_y/\lambda_x$. However, all three are retained in the analysis for ease of exposition.

Following the GKS approach, we look for solutions of (44) of the form

$$\begin{bmatrix} \tilde{u}^n_{1,j} \\ \tilde{u}^n_{2,j} \\ \tilde{p}^n_j \end{bmatrix} = a^n \begin{bmatrix} \tilde{u}_{1,j} \\ \tilde{u}_{2,j} \\ \tilde{p}_j \end{bmatrix} = a^n\kappa^j \begin{bmatrix} U \\ V \\ P \end{bmatrix}, \tag{46}$$

that grow exponentially in time, i.e. $|a| > 1$, where (U, V, P) are constants. Our goal will be to show that there are no unstable solutions satisfying the discrete scheme and boundary conditions with $|a| > 1$. Substituting the ansatz in (46) for $\tilde{p}^n_j$ into the scaled pressure equation (44c) leads to the characteristic equation

$$\kappa^2 - 2(1 + z_p/2)\kappa + 1 = 0, \tag{47}$$

where

$$z_p \stackrel{\text{def}}{=} -\mathcal{R}^2\,\widehat{\delta_{yy}} \geq 0. \tag{48}$$

Note that when $z_p = 0$ there is a double root $\kappa = 1$ of (47) which then leads to a solution of the form $\tilde{p}_j = P_1 + jP_2$ for constants P_1 and P_2. For boundedness $P_2 = 0$. The remaining constant solution for the pressure causes no issues and is not considered further. The product of the roots to (47) is one, and when $z_p > 0$ there is one root with magnitude greater than one while the other root has magnitude less than one. Define

$$\varkappa_p \stackrel{\text{def}}{=} 1 + z_p/2 - \sqrt{z_p}\sqrt{1 + z_p/4}, \tag{49}$$

where the principle branch of the square root is assumed. We note that $\kappa = \varkappa_p$ is the root with magnitude less than one for any positive z_p (see [34]), which implies that $1/\varkappa_p$ is the other root. Thus, the general solution to (42c) takes the form

$$\tilde{p}_j^n = a^n \left(P_1\, \varkappa_p^j + P_2\, \varkappa_p^{-j}\right), \tag{50}$$

and requiring boundedness for $j \to \infty$ implies $P_2 = 0$, and so

$$\tilde{p}_j^n = P\, a^n \varkappa_p^j, \tag{51}$$

where P is a complex constant yet to be determined (with the subscript dropped for notational convenience).

To find the solution to (44a) we again use the ansatz in (46), and upon rearranging we find

$$(\alpha_x\, \delta_{+x}\delta_{-x} + \alpha_y\, \widehat{\delta_{yy}} - \ s_2^2)\, \tilde{u}_{1,j} = \delta_{0x}\, \tilde{p}_j, \tag{52}$$

where

$$\alpha_d \stackrel{\text{def}}{=} \lambda_d\, (\lambda_d + \beta s_1), \qquad d = x, y, \tag{53}$$

and s_1, the symbol of δ_{-t}, and s_2^2, the symbol of $\delta_{+t}\delta_{-t}$, are given by

$$s_1 \stackrel{\text{def}}{=} 1 - a^{-1}, \tag{54a}$$

$$s_2^2 \stackrel{\text{def}}{=} a - 2 + a^{-1}. \tag{54b}$$

The solution to (52) consists of a homogeneous solution and a particular solution. The homogeneous solution $(\tilde{u}_{1,j}^n)_h$ has the form in (46) with κ solving the characteristic equation

$$\kappa^2 - 2(1 + z/2)\kappa + 1 = 0, \tag{55}$$

where

$$z \stackrel{\text{def}}{=} \frac{1}{\alpha_x}(s_2^2 - \alpha_y \widehat{\delta_{yy}}). \tag{56}$$

The product of the two roots of (55) is one, and when $|a| > 1$ there must be one root with $|\kappa| < 1$. To see this, note that if $|\kappa| = 1$, say $\kappa = e^{i\theta}$, we have $z = \kappa - 2 + \kappa^{-1} = -4\sin^2(\theta/2)$ from (55), and then

$$s_2^2 = a - 2 + a^{-1} = \alpha_x(-4\sin^2(\theta/2)) + \alpha_y \widehat{\delta_{yy}}. \tag{57}$$

using (56). But (57) is equivalent to the equation for a found in the analysis of the spatially periodic problem in Appendix B, c.f. (B.5a). In that analysis, it is assumed that Δt is chosen to make the

spatially periodic problem stable, and this implies $|a| \leq 1$. Therefore in our current analysis which assumes $|a| > 1$, it cannot be that $|\kappa| = 1$, and thus there must be one root with $|\kappa| > 1$ and a second root with $|\kappa| < 1$. Denote the root with $|\kappa| < 1$ by

$$\varkappa \stackrel{\text{def}}{=} 1 + z/2 - \sqrt{z}\sqrt{1 + z/4}. \tag{58}$$

Imposing the solution to be bounded as $j \to \infty$ implies the homogeneous solution is given by

$$(\tilde{u}^n_{1,j})_h = U\, a^n\, \varkappa^j, \tag{59}$$

where U is a constant yet to be determined. The particular solution of (52) can be found by substituting the ansatz

$$(\tilde{u}^n_{1,j})_p = U_p\, a^n\, \varkappa_p^j, \tag{60}$$

into (52) which leads to $U_p = P\gamma_x$, where

$$\gamma_x \stackrel{\text{def}}{=} \frac{\lambda_x \eta_p}{s_1\, \beta\, \lambda_y\, \widehat{\delta_{yy}}\, (1 - \mathcal{R}) - s_2^2}. \tag{61}$$

Here, we have defined

$$\eta_p \stackrel{\text{def}}{=} \frac{\varkappa_p - \varkappa_p^{-1}}{2}, \tag{62}$$

and in what follows it is also convenient to make the analogous definition

$$\eta \stackrel{\text{def}}{=} \frac{\varkappa - \varkappa^{-1}}{2}. \tag{63}$$

Summing the solutions in (59) and (60) gives the general solution

$$\tilde{u}^n_{1,j} = a^n\, (U\, \varkappa^j + P\gamma_x\, \varkappa_p^j). \tag{64}$$

A similar analysis for the scaled displacement in the y direction leads to

$$\tilde{u}^n_{2,j} = a^n\, (V\, \varkappa^j + P\gamma_y\, \varkappa_p^j), \tag{65}$$

where V is a complex constant, and

$$\gamma_y \stackrel{\text{def}}{=} \frac{\lambda_y \widehat{\delta_y}}{s_1\, \beta\, \lambda_y\, \widehat{\delta_{yy}}\, (1 - \mathcal{R}) - s_2^2}. \tag{66}$$

Thus, the full general solution, assuming $|a| > 1$ and boundedness as $j \to \infty$, is given by

$$\tilde{u}^n_{1,j} = a^n\, (U\, \varkappa^j + P\gamma_x\, \varkappa_p^j), \tag{67a}$$
$$\tilde{u}^n_{2,j} = a^n\, (V\, \varkappa^j + P\gamma_y\, \varkappa_p^j), \tag{67b}$$
$$\tilde{p}^n_j = a^n\, P\, \varkappa_p^j, \tag{67c}$$

where $\varkappa_p$ and $\varkappa$ are given in (49) and (58), respectively, and the constants γ_x and γ_y are given in (61) and (66). Note that the solution depends on the three free constants (U, V, P). It remains to consider the boundary conditions on $j = 0$ corresponding to $x = 0$.

Displacement Boundary Conditions. Consider now the case of homogeneous displacement boundary conditions, which are discretized in (19), and here take the form

$$\tilde{u}^n_{1,0} = 0, \tag{68a}$$
$$\tilde{u}^n_{2,0} = 0, \tag{68b}$$
$$\delta_{0x}\tilde{u}^n_{1,0} + \mathcal{R}\,\widehat{\delta}_y \tilde{u}^n_{2,0} = 0. \tag{68c}$$

We will show the following result.

Theorem 3 (Displacement boundary conditions)**.** *The scheme (39) with displacement boundary conditions (68) is stable (i.e. admits no exponentially growing modes) under the time-step restrictions implied by Theorem 2. In particular, the scheme is stable with or without upwinding.*

Proof. Substituting the general solution in (67) into (68) yields the homogeneous system

$$A_d \mathbf{w} = 0, \tag{69}$$

where

$$A_d = \begin{bmatrix} 1 & 0 & \gamma_x \\ 0 & 1 & \gamma_y \\ \eta & \mathcal{R}\widehat{\delta}_y & \gamma_x\eta_p + \mathcal{R}\widehat{\delta}_y\gamma_y \end{bmatrix}, \qquad \mathbf{w} = \begin{bmatrix} U \\ V \\ P \end{bmatrix}. \tag{70}$$

Nontrivial solutions can exist if

$$\mathcal{D}_d(a) \stackrel{\text{def}}{=} \det(A_d) = \gamma_x(a)\,(\eta(a) - \eta_p) = 0, \tag{71}$$

where the dependence of the determinant $\mathcal{D}_d$ on the amplification factor a can be traced from

$$\gamma_x(a) \stackrel{\text{def}}{=} \frac{\lambda_x \eta_p}{s_1(a)\,\beta\,\lambda_y\,\widehat{\delta_{yy}}\,(1-\mathcal{R}) - s_2^2(a)}, \tag{72a}$$
$$\eta(a) \stackrel{\text{def}}{=} \frac{\varkappa(a) - \varkappa(a)^{-1}}{2}, \tag{72b}$$
$$s_1(a) \stackrel{\text{def}}{=} 1 - a^{-1}, \tag{72c}$$
$$s_2^2(a) \stackrel{\text{def}}{=} a - 2 + a^{-1}, \tag{72d}$$
$$\varkappa(a) \stackrel{\text{def}}{=} 1 + z(a)/2 - \sqrt{z(a)}\sqrt{1 + z(a)/4}, \tag{72e}$$
$$z(a) \stackrel{\text{def}}{=} \frac{1}{\alpha_x}(s_2^2(a) - \alpha_y \widehat{\delta_{yy}}). \tag{72f}$$

Note that $\gamma_x = 0$ implies $\eta_p = 0$ from the definition in (61), which in turn implies $\varkappa_p = \pm 1$ from (62). However, since $|\varkappa_p| < 1$, we conclude that $\gamma_x \neq 0$. This leaves $\eta = \eta_p$, which reduces to

$$\sqrt{z}\sqrt{1 + z/4} = \sqrt{z_p}\sqrt{1 + z_p/4}, \tag{73}$$

using (62) and (63), and then the definitions of $\varkappa_p$ and $\varkappa$ in (49) and (58), respectively.

After squaring (73) one finds two possible solutions, $z = z_p$ and $z = -(4 + z_p)$, with the latter discarded since it is not a solution to the original constraint in (73). The only solution is thus $z = z_p$ which implies $\varkappa = \varkappa_p$, and then the solutions in (67) for the scaled displacements simplify to

$$\tilde{u}^n_{1,j} = a^n\,(U + P\gamma_x)\varkappa_p^j = a^n\,\bar{U}\varkappa_p^j, \tag{74a}$$
$$\tilde{u}^n_{2,j} = a^n\,(V + P\gamma_y)\varkappa_p^j = a^n\,\bar{V}\varkappa_p^j. \tag{74b}$$

The displacement boundary conditions (68), then, imply

$$\bar{U} = 0, \tag{75a}$$
$$\bar{V} = 0, \tag{75b}$$
$$\bar{U}(\varkappa - \varkappa^{-1}) + \mathcal{R}\,\widehat{\delta}_y \bar{V} = 0. \tag{75c}$$

The only solution is the trivial solution $\bar{U} = \bar{V} = 0$, which implies $\tilde{u}^n_{1,j} = \tilde{u}^n_{2,j} = 0$. Whence there are no unstable modes for the case of displacement boundary conditions, even when $\beta = 0$ and there is no added dissipation. This completes the proof.

□

Traction Boundary Conditions. The components of the discretized (and scaled) traction boundary condition in (24) at $x = 0$ can be expressed as

$$\delta_{0x}\tilde{u}^n_{1,0} + \mathcal{R}\,\widehat{\delta}_y \tilde{u}^n_{2,0} = 0, \tag{76a}$$
$$\delta_{0x}\tilde{u}^n_{2,0} + \mathcal{R}\,\widehat{\delta}_y \tilde{u}^n_{1,0} = 0, \tag{76b}$$
$$\tilde{p}^n_0 + 2\lambda_y\,\widehat{\delta}_y \tilde{u}^n_{2,0} = 0. \tag{76c}$$

We will show the following result.

Theorem 4 (Traction boundary conditions)**.** *The scheme* (39) *with traction boundary conditions* (76)*, and assuming* $\mathcal{R} = \Delta x/\Delta y = \lambda_y/\lambda_x = 1$*, is stable (i.e. admits no exponentially growing modes) under a time-step restriction close to that implied by Theorem 2 provided the upwind parameter is larger than some critical value,* $\beta \geq \beta_c \approx 0.1$*. The approximate region of stability as a function of* β *is given in Figure 6.*

The proof consists of a GKS analysis leading to a determinant condition whose roots indicate any instabilities. The determinant condition is investigated numerically to derive conclusions. Substituting the general solution (67) into the scaled traction boundary conditions (76) yields

$$U\eta + \gamma_x P\eta_p + \mathcal{R}\widehat{\delta}_y(V + \gamma_y P) = 0, \tag{77a}$$
$$V\eta + \gamma_y P\eta_p + \mathcal{R}\widehat{\delta}_y(U + \gamma_x P) = 0, \tag{77b}$$
$$P + 2\lambda_y\,\widehat{\delta}_y(V + \gamma_y P) = 0, \tag{77c}$$

which implies the homogeneous system

$$A_\tau \mathbf{w} = 0, \tag{78}$$

where

$$A_\tau = \begin{bmatrix} \eta & \mathcal{R}\widehat{\delta}_y & \eta_p\gamma_x + \mathcal{R}\widehat{\delta}_y\gamma_y \\ \mathcal{R}\widehat{\delta}_y & \eta & \eta_p\gamma_y + \mathcal{R}\widehat{\delta}_y\gamma_x \\ 0 & 2\lambda_y\widehat{\delta}_y & 1 + 2\lambda_y\widehat{\delta}_y\gamma_y \end{bmatrix}, \qquad \mathbf{w} = \begin{bmatrix} U \\ V \\ P \end{bmatrix}. \tag{79}$$

Nontrivial solutions exist if

$$\mathcal{D}_\tau(a) \stackrel{\text{def}}{=} \det(A_\tau) = 0 \tag{80}$$

where, as in the case of displacement boundaries the dependence of the determinant condition on a can be found by tracing the definitions (72). Note that the determinant $\mathcal{D}_\tau(a)$ depends on

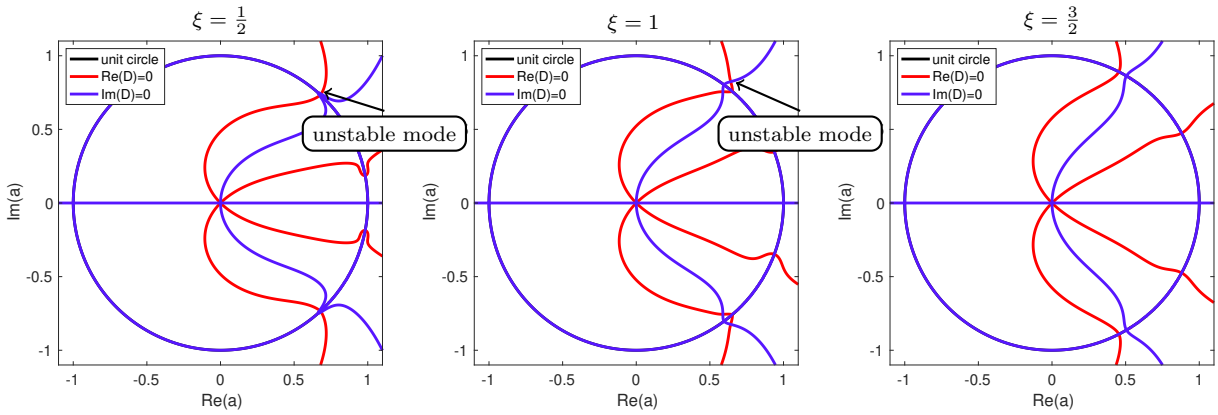

Figure 3: Plots of the zero contours of the real and imaginary parts of $\mathcal{D}(a)$ with $\beta = 0$, $\lambda_x = \lambda_y = .4$, and $\xi = \frac{1}{2}$ (left), $\xi = 1$ (center), and $\xi = \frac{3}{2}$ (right). Instability is indicated for both $\xi = \frac{1}{2}$ and $\xi = 1$, while for $\xi = \frac{3}{2}$ there is no instability observed.

the "CFL" parameters (λ_x, λ_y), the transverse wave number $\xi = k\Delta y \in [-\pi, \pi]$, and the upwind parameter β. For the subsequent analysis we assume $\lambda = \lambda_x = \lambda_y$ so that $\mathcal{D}_\tau(a)$ depends on the parameters (λ, ξ, β). Roots of $\mathcal{D}_\tau(a) = 0$ with $|a| > 1$ correspond to unstable exponentially growing solutions in time, whereas if there are no roots with $|a| > 1$ (and assuming a stable time-step for the Cauchy problem with periodic boundaries is chosen), then the half-plane problem with traction boundary conditions is stable.

Figure 3 addresses the question of stability in the non-dissipative scheme with $\beta = 0$. Here the zero-contours of the real and imaginary parts of the determinant $\mathcal{D}_\tau(a)$ are plotted in the complex a-plane for various values of the wave number ξ and for a fixed $\lambda = 0.4$. Intersections of these two zero-contours indicate solutions of $\mathcal{D}_\tau(a) = 0$, and those solutions lying outside of the unit circle correspond to exponentially growing unstable modes. For both $\xi = \frac{1}{2}$ and $\xi = 1$, unstable modes are observed, although for $\xi = \frac{1}{2}$ the mode lies only slightly outside the unit circle and is difficult to make out visually. In particular, for $\xi = \frac{1}{2}$ the solution to 10-digit accuracy is $a = 0.6837836151 + 0.7400650665i$ with $|a| = 1.007599293$, and for $\xi = 1$ the solution to 10-digit accuracy is $0.6413787362 + 0.8241473570i$ with $|a| = 1.044311040$. On the other hand, no unstable modes are seen for $\xi = \frac{3}{2}$. Unlike the case of displacement boundary conditions, it is apparent that the scheme is unstable with traction boundary conditions.

The effect of upwind dissipation is to stabilize the scheme for a fixed discrete wave number, and this is illustrated in Figure 4. Again, zero-contours of the real and imaginary parts of $\mathcal{D}_\tau(a)$ are plotted to reveal roots of the determinant condition, and this is done here for $\xi = 1$ and $\lambda = 0.4$, and for various choices of the dissipation parameter given by $\beta = 0.02$, 0.06125 and 0.15. For $\beta = 0.02$ an instability is still observed with $a = 0.6239926549 + 0.8190060126i$ and $|a| = 1.029629876$ (again to 10 digits). However, for $\beta = 0.06125$ and 0.15, the scheme appears to be stable as all roots of $\mathcal{D}(a) = 0$ lie inside the unit circle.

The indication from Figures 3 and 4 and related discussion is a relationship between a minimum value of β required for stability and the discrete wave number ξ. This relationship is investigated in Figure 5 which shows the maximum $|a|$ for all unstable cases as a function of β and ξ. Here we see that the most unstable mode, in the sense of largest $|a|$ is observed for $\xi \approx 1$, and that this instability is suppressed for $\beta \gtrapprox 0.06$. The results so far have been for $\lambda = 0.4$. We next investigate a wider class of parameters.

An approximate stability region can be found numerically as follows. The determinant condition $\mathcal{D}_\tau(a) = 0$ is not a polynomial in a since it involves square-roots of a through the definitions of κ and κ_p. However, using standard algebraic manipulations, a related polynomial constraint,

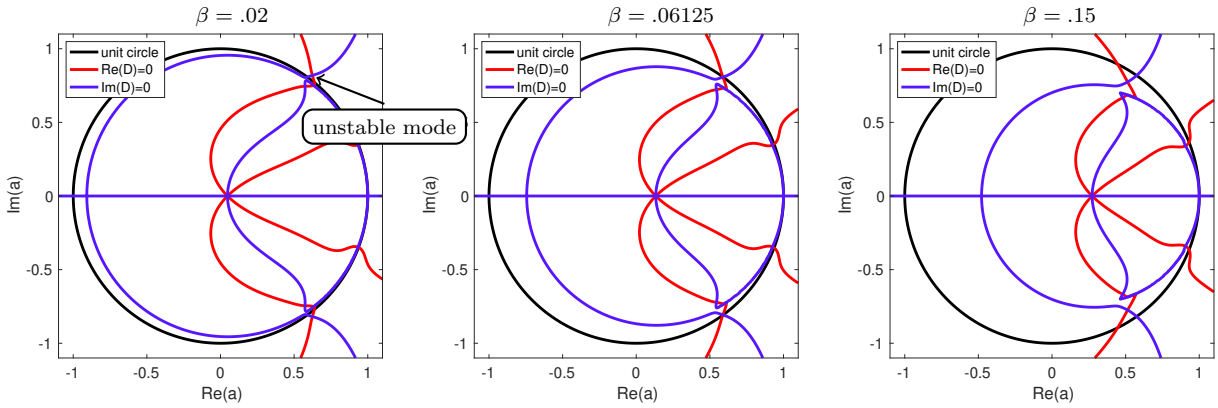

Figure 4: Plots of the zero contours of the real and imaginary parts of $\mathcal{D}(a)$ with $k = 1$, $\lambda_x = \lambda_y = .4$, and $\beta = 0.02$ (left), $\beta = 0.06125$ (center), and $\beta = 0.15$ (right). Instability is indicated only for $\beta = 0.02$, while for $\beta = 0.06125$ and $\beta = 0.15$ there is no instability observed.

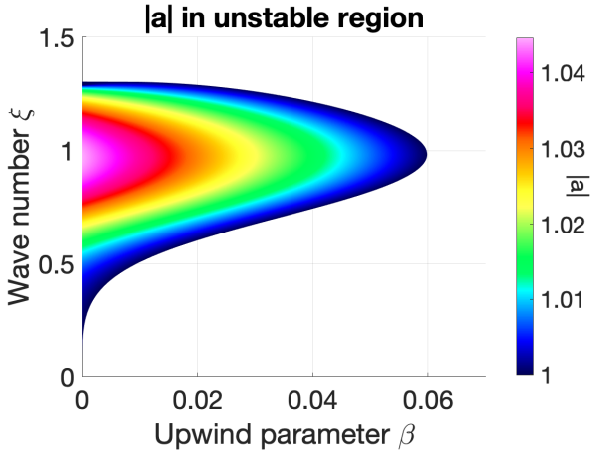

Figure 5: Magnitude of the amplification factor, $|a|$, for unstable modes as a function of the upwind parameter β and wave number ξ, for $\lambda_x = \lambda_y = 0.4$.

$\mathcal{P}_\tau(a) = 0$, can be found whose roots include all of the roots of $\mathcal{D}_\tau(a) = 0$, but also additional spurious roots. In this case the polynomial is of degree twelve. It is straightforward to find all roots of $\mathcal{P}_\tau(a) = 0$ and then eliminate the spurious roots by checking whether $\mathcal{D}_\tau(a) = 0$ is satisfied for each root. For each value of λ and β we can find the magnitude of the largest root a over all $|\xi| \le \pi$,

$$\mathcal{A}(\beta, \lambda) = \max_{|\xi| \le \pi} \Big\{ |a| \ : \ \mathcal{D}_\tau(a;\, \lambda, \xi, \beta) = 0 \Big\}. \tag{81}$$

Regions where $\mathcal{A}(\beta, \lambda_x) \le 1$ are deemed to be stable, while regions where $\mathcal{A}(\beta, \lambda_x) > 1$ are considered to be unstable. In practice we check a finite number of values for ξ when computing the maximum and include some tolerances. Using a symbolic algebra program, such as Maple, with extended precision arithmetic yields acceptable results.

Figure 6 shows the approximate stability region as a function of β and the CFL number defined as

$$\text{CFL} \stackrel{\text{def}}{=} \sqrt{\lambda_x^2 + \lambda_y^2} = \sqrt{2}\,\lambda, \tag{82}$$

for $\lambda_x = \lambda_y = \lambda$. The scheme is found to be stable at the green circles and unstable at the red x's. A value of $\beta = 0.1$ is nearly optimal as it provides stability for the largest range of CFL numbers.

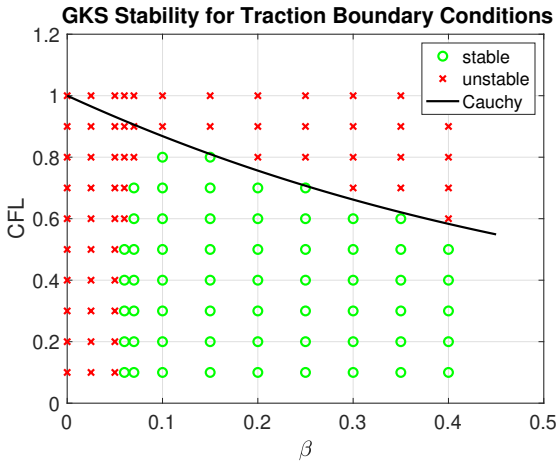

Figure 6: GKS stability for the model problem with traction boundary conditions. The scheme was found to be stable at the green circles and unstable at the red x's. The black line indicates the stability bound for the Cauchy problem with periodic boundary conditions.

The black solid curve shows the time-step restriction implied by the Cauchy problem (2). This curve, denoted by $\mathrm{CFL}_{\max}(\beta)$, is determined by solving for the positive root of

$$\lambda_x^2 + \lambda_y^2 + 2\beta(\lambda_x + \lambda_y) - 1 = 2\lambda^2 + 4\beta\lambda - 1 = 0, \tag{83}$$

which is given by $\lambda(\beta) = -\beta + \sqrt{\beta^2 + \frac{1}{2}}$ and then using (82) to obtain

$$\mathrm{CFL}_{\max}(\beta) = \sqrt{2}\lambda(\beta) = \sqrt{1 + 2\beta^2} - \sqrt{2}\,\beta. \tag{84}$$

As β increases past $\beta \approx 0.1$ and until the maximum allowable β ($\beta_{\max} = 1/(4\lambda)$ given by (41)), the scheme is stable but at a reduced CFL number. Note that this reduction in the CFL number is associated with the particular scheme being used for this analysis; there is no such reduction in the actual schemes, which add upwinding in a predictor-corrector manner as discussed in Section 3.4.

Finally, note that the results here are presented for $\lambda_x = \lambda_y$ which corresponds to $\mathcal{R} = 1$. We have observed that varying $\mathcal{R}$ does have some effect on the results, and in particular we find that instability can occur for $\mathcal{R}$ sufficiently large. Our current experiments indicate that the limit for the second-order accurate SOS-ME scheme is $\mathcal{R} \approx 2$, but a more detailed investigation of this phenomena is required and this will be the subject of future work.

5. Curvilinear grids, mappings, and overset grids

To solve problems on complex geometry the new schemes have been implemented for overset grids, also known as a Chimera or composite overlapping grids. As illustrated in Figure 7, an overset grid, denoted as $\mathcal{G}$, consists of a set of component grids $\{G_g\}$, $g = 1, \ldots, \mathcal{N}$, that cover the entire domain Ω. The primary motivation for our use of composite overlapping grids is to enable the use of efficient finite difference schemes on structured grids, while simultaneously treating complex geometry with high-order accuracy up to and including boundaries. In three dimensions, each component grid, G_g, is a logically rectangular, curvilinear grid defined by a smooth mapping from a unit cube parameter space $\mathbf{r}$ to physical space $\mathbf{x}$,

$$\mathbf{x} = \mathbf{G}_g(\mathbf{r}), \qquad \mathbf{r} \in [0,1]^3, \qquad \mathbf{x} \in \mathbb{R}^3. \tag{85}$$

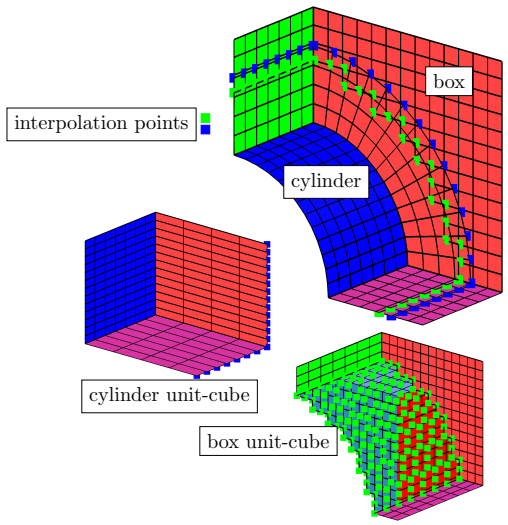

Figure 7: Top: a three-dimensional overlapping grid for a quarter-cylinder in a box. Bottom left and right: component grids for the cylindrical and box grids in the unit cube parameter space. Interpolation points at the grid overlap are marked and color-coded for each component grid.

All grid points in $\mathcal{G}$ are classified as discretization, interpolation or unused points [35]. The overlapping grid generator **Ogen** [36] from the *Overture* framework is used to construct the overlapping grid information. In a typical composite grid, one or more boundary-fitted curvilinear grids represent each boundary. The remainder of the domain is covered by one or more Cartesian grids. **Ogen** cuts holes in the appropriate component grids by using physical boundaries to distinguish between the interior and exterior to the domain. Grid points outside the domain are classified as unused points. For instance, the "cylinder" grid displayed in the upper right image of Figure 7 cuts a hole in the Cartesian "box" grid so that the latter grid has many unused points (those not being plotted in the lower right image). **Ogen** also provides the interpolation information for all interpolation points in the overlap region between component grids. The interpolation between grids is defined using tensor-product Lagrange interpolation in the parameter space of the mapping $\mathbf{G}$. The unit square coordinates $\mathbf{r}$ of a given point $\mathbf{x}$ on one grid are located in the donor-grid parameter space. The interpolation is performed in the Cartesian-grid parameter space and is thus straightforward [35]. For second-order accuracy, one layer of interpolation points is required to support the three-point stencil. A three-point interpolation stencil (in each direction) is used, as required for second-order accuracy on typical grids [35].

Forming approximations to derivatives on a Cartesian grid is straightforward. Let $\mathbf{x}_\mathbf{i}$ denote the grid points, where $\mathbf{i} = [i_1, i_2, i_3]$ is a multi-index and $i_m = 0, 1, \ldots, N_m$, where N_m is the number of grid cells in m^{th} direction. Let $\Delta x_m = 1/N_m$ denote the grid spacing with $\mathbf{x}_\mathbf{i} = (i_1\Delta x_1, i_2\Delta x_2, i_3\Delta x_3)$. Let $u_\mathbf{i} \approx u(\mathbf{x}_\mathbf{i})$ and define the standard divided difference operators,

$$D_{+x_m} u_\mathbf{i} \stackrel{\text{def}}{=} \frac{u_{\mathbf{i}+\mathbf{e}_m} - u_\mathbf{i}}{\Delta x_m}, \qquad D_{-x_m} u_\mathbf{i} \stackrel{\text{def}}{=} \frac{u_\mathbf{i} - u_{\mathbf{i}-\mathbf{e}_m}}{\Delta x_m}, \qquad D_{0x_m} u_\mathbf{i} \stackrel{\text{def}}{=} \frac{u_{\mathbf{i}+\mathbf{e}_m} - u_{\mathbf{i}-\mathbf{e}_m}}{2\Delta x_m}. \tag{86}$$

Second-order accurate approximations to the Laplacian and gradient in Cartesian coordinates are then

$$\Delta_h \stackrel{\text{def}}{=} \sum_{m=1}^{n_d} D_{+x_m} D_{-x_m}, \tag{87}$$

$$\nabla_h \stackrel{\text{def}}{=} [D_{0,x_1}, D_{0,x_2}, D_{0,x_3}]^T. \tag{88}$$

Forming approximations to derivatives on a curvilinear grid is a bit more complicated and there are several ways to approach this; here we use the *mapping method*. Given a mapping $\mathbf{x} = \mathbf{G}_g(\mathbf{r})$ and its metric derivatives, $\partial r_\ell/\partial x_m$, $1 \le \ell, m \le n_d$, the derivatives of a function $u(\mathbf{x}) = U(\mathbf{r})$ are first written in parameter space using the chain rule, for example,

$$\frac{\partial u}{\partial x_m} = \sum_{\ell=1}^{n_d} \frac{\partial r_\ell}{\partial x_m} \frac{\partial U}{\partial r_\ell}. \tag{89}$$

Derivatives of U with-respect to r_ℓ are then approximated with standard finite differences. Let $\mathbf{r_i}$ denote grid points on the unit square, where $i_k = 0, 1, \ldots, N_k$. Let $\Delta r_k = 1/N_k$ denote the grid spacing on the unit cube with $\mathbf{r_i} = (i_1 \Delta r_1, i_2 \Delta r_2, i_3 \Delta r_3)$. Let $U_\mathbf{i} \approx U(\mathbf{r_i})$ and define the difference operators,

$$D_{+r_\ell} U_\mathbf{i} \stackrel{\text{def}}{=} \frac{U_{\mathbf{i}+\mathbf{e}_\ell} - U_\mathbf{i}}{\Delta r_\ell}, \qquad D_{-r_\ell} U_\mathbf{i} \stackrel{\text{def}}{=} \frac{U_\mathbf{i} - U_{\mathbf{i}-\mathbf{e}_\ell}}{\Delta r_\ell}, \quad D_{0r_\ell} U_\mathbf{i} \stackrel{\text{def}}{=} \frac{U_{\mathbf{i}+\mathbf{e}_\ell} - U_{\mathbf{i}-\mathbf{e}_\ell}}{2\Delta r_\ell}, \tag{90}$$

where $\mathbf{e}_\ell$ is the unit vector in direction ℓ (e.g. $\mathbf{e}_2 = [0, 1, 0]$). Second-order accurate approximations to the first derivatives are

$$D_{x_m,h} U_\mathbf{i} \stackrel{\text{def}}{=} \sum_{\ell=1}^{n_d} \left.\frac{\partial r_\ell}{\partial x_m}\right|_\mathbf{i} D_{0,r_\ell} U_\mathbf{i}, \tag{91}$$

where we assume the metric terms $\partial r_\ell/\partial x_m$ are known at grid points from the mapping. We do not, however, assume the second derivatives of the mapping are known (to avoid the extra storage) and these are computed using finite differences of the metrics. Using the chain rule, the second derivatives are

$$\frac{\partial^2 u}{\partial x_m \partial x_n} = \sum_{k=1}^{n_d} \sum_{l=1}^{n_d} \frac{\partial r_k}{\partial x_m} \frac{\partial r_l}{\partial x_n} \frac{\partial^2 U}{\partial r_k \partial r_l} + \sum_{k=1}^{n_d} \left\{ \sum_{l=1}^{n_d} \frac{\partial r_l}{\partial x_n} \frac{\partial}{\partial r_l} \frac{\partial r_k}{\partial x_m} \right\} \frac{\partial U}{\partial r_k}. \tag{92}$$

The second derivatives are approximated to second-order accuracy using approximations such as

$$\left.\frac{\partial^2 U}{\partial r_k \partial r_l}\right|_{\mathbf{r_i}} \approx D_{+r_k} D_{-r_l} U_\mathbf{i}, \qquad \text{for } k = l, \tag{93}$$

$$\left.\frac{\partial^2 U}{\partial r_k \partial r_l}\right|_{\mathbf{r_i}} \approx D_{0r_k} D_{0r_l} U_\mathbf{i}, \qquad \text{for } k \ne l, \tag{94}$$

$$\left.\frac{\partial}{\partial r_l}\left(\frac{\partial r_k}{\partial x_m}\right)\right|_{\mathbf{r_i}} \approx D_{0r_l}\left(\left.\frac{\partial r_k}{\partial x_m}\right|_\mathbf{i}\right). \tag{95}$$

On a curvilinear grid the upwind dissipation, introduced in Section 3.4, is taken as

$$\mathbf{U}_\mathbf{i}^{n+1} = \mathbf{U}_\mathbf{i}^{p} - \Delta t^2 \beta_4 \sum_{k=1}^{n_d} \frac{c\,\|\nabla_\mathbf{x} r_k\|}{\Delta r_k} \left(\Delta_{+r_k} \Delta_{-r_k}\right)^2 \left(\frac{\mathbf{U}_\mathbf{i}^{p} - \mathbf{U}_\mathbf{i}^{n-1}}{2\Delta t}\right), \tag{96a}$$

$$\|\nabla_\mathbf{x} r_k\|^2 = \sum_{m=1}^{n_d} \left[\frac{\partial r_k}{\partial x_m}\right]^2. \tag{96b}$$

Here Δ_{+r_k} and Δ_{-r_k} are the usual undivided difference approximations in the parameter space $\mathbf{r}$.

6. Numerical results

In this section we present numerical results to demonstrate the accuracy and stability of the proposed fractional-step schemes. Results are shown for a number of problems in two- and three-dimensions where exact solutions can be found. We focus on problems with smooth solutions so that the accuracy of the schemes can be assessed. We start by showing convergence results using manufactured solutions in Section 6.1. This demonstrates the use of inhomogeneous forcing and boundary conditions. Section 6.2 provides results for exact solutions on a periodic strip in two and three space dimensions. This is a good test case in a simple geometry for assessing stability with traction and displacement boundary conditions. Section 6.3 shows results for exact solutions on an annulus; which is a good test for a simple curvilinear domain. Section 6.3 also presents convergence results for exact solutions on a disk which is a good test for overset grids in two dimensions. Section 6.4 considers exact solutions on a three dimensional hollow and solid cylinder; these are good tests for three-dimensional problems. Section 6.5 considers vibrational modes of a solid sphere which is another good test case with exact solutions in three dimensions. Note that derivation of exact solutions required for the tests presented in Section 6.2–6.5 represents a non-trivial effort, and represents one of the contributions of this manuscript. Therefore, sufficient details are included to aid those readers wishing to reproduce the results shown here, or to test their own numerical algorithms. We conclude the numerical results in Section 6.6 with some very long-time simulations that provide a severe test of the stability of the schemes.

6.1. Manufactured solutions

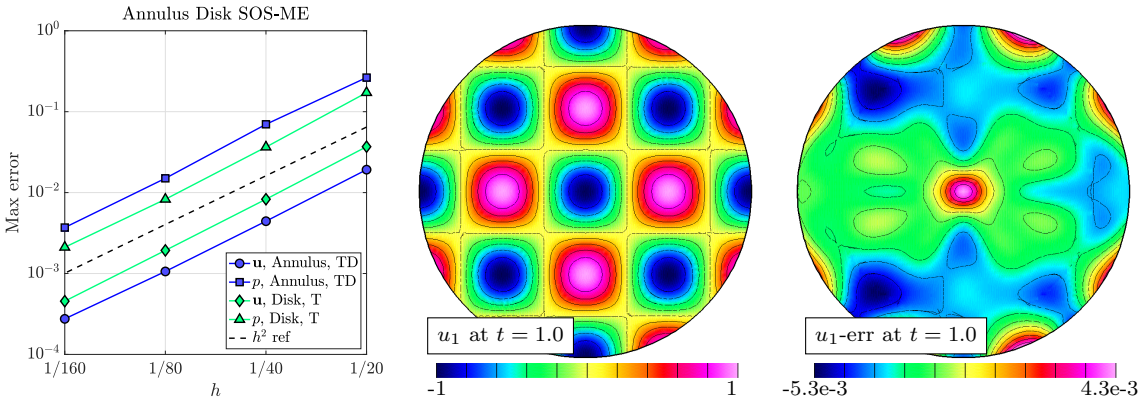

Figure 8: Manufactured solution results. Left: grid convergence for an annulus and disk. Middle: solution u_1. Right: error in u_1.

In this section we present results using trigonometric manufactured solutions of the form

$$u_1(\mathbf{x},t) = \cos(kx_1)\cos(kx_2)\cos(\omega t), \tag{97a}$$
$$u_2(\mathbf{x},t) = \sin(kx_1)\sin(kx_2)\cos(\omega t), \tag{97b}$$
$$p(\mathbf{x},t) = \cos(kx_1)\cos(kx_2)\cos(\omega t), \tag{97c}$$

with $k = 2\pi$, and $\omega = \pi$. Note that the displacement, $\mathbf{u} = (u_1, u_2)$, of the manufactured solution is divergence free. Forcing functions are added to the governing equations (5) to make this an exact solution. Inhomogeneous boundary conditions are also specified to be consistent with (97).

Figure 8 shows grid convergence results for an annulus and a disk where max-norm errors are plotted as a function of grid resolution. Definitions of the grids are given in Section 6.3. For the

annular case, a traction boundary condition is applied on the inner radius and a displacement boundary condition is applied on the outer radius. For the case of the disk, a traction boundary condition is used. All results were computed using $\rho = 1$ and $\mu = 1$. The figure also shows contours of the solution and error for component u_1 for the disk domain using grid $\mathcal{G}_d^{(4)}$ (as defined in Section 6.3). Convergence results indicate that both the displacements and pressure are converging at close to second-order accuracy, and the contours of the error show excellent smooth behavior throughout the domain.

6.2. Eigenmodes in a periodic channel

Exact eigenmodes of the incompressible elasticity equations on the cube domain, $\Omega = [0,1]^3$, periodic in y and z, can be found for various combinations of traction or displacement boundary conditions at $x = 0$ and $x = 1$. The solutions take the form

$$\begin{bmatrix} \mathbf{u}(\mathbf{x},t) \\ p(\mathbf{x},t) \end{bmatrix} = \begin{bmatrix} \hat{\mathbf{u}}(x) \\ \hat{p}(x) \end{bmatrix} e^{i(k_y y + k_z z)}\, e^{i\omega t}, \tag{98}$$

where ω is a frequency in time, and $(k_y, k_z) = 2\pi\,(m_y, m_z)$, for integers m_y and m_z, are wave numbers in the (y,z) directions. The functions $\hat{\mathbf{u}}(x) = (\hat{u}_1, \hat{u}_2, \hat{u}_3)^T = (\hat{u}_1, i\tilde{u}_2, i\tilde{u}_3)^T$ and $\hat{p}(x)$ are given by

$$\hat{u}_1(x) = A_1 \cos\beta x + B_1 \sin\beta x + \frac{1}{\mu(\beta^2 + k^2)}\hat{p}'(x), \tag{99a}$$

$$\tilde{u}_2(x) = A_2 \cos\beta x + B_2 \sin\beta x + \frac{k_y}{\mu(\beta^2 + k^2)}\hat{p}(x), \tag{99b}$$

$$\tilde{u}_3(x) = A_3 \cos\beta x + B_3 \sin\beta x + \frac{k_z}{\mu(\beta^2 + k^2)}\hat{p}(x), \tag{99c}$$

$$\hat{p}(x) = P_1 e^{kx} + P_2 e^{-kx}, \tag{99d}$$

where (A_ℓ, B_ℓ), $\ell = 1,2,3$, and (P_1, P_2) are constants, and k and β are specified by

$$k^2 \stackrel{\text{def}}{=} k_y^2 + k_z^2, \tag{100a}$$

$$\beta^2 \stackrel{\text{def}}{=} \frac{\omega^2}{c^2} - k^2. \tag{100b}$$

Note that the variables $\tilde{u}_2$ and $\tilde{u}_3$ are introduced so that in the most common situation when β is real-valued, the constants (A_ℓ, B_ℓ) and (P_1, P_2) are real-valued as well. Also note that the zero-divergence condition implies

$$\tilde{u}_3(x) = \frac{1}{k_z}\big(\hat{u}_1'(x) - k_y\,\tilde{u}_2(x)\big), \tag{101}$$

assuming $k_z \neq 0$ and this can be used to define A_3 and B_3 in terms of the other constants for three-dimensional problems. For two-dimensional problems, or when $k_z = 0$, one can take

$$\tilde{u}_2 = \frac{\hat{u}_1'(x)}{k_y}, \tag{102}$$

assuming $k_y \neq 0$ to define A_2 and B_2 in terms of the other constants. Homogeneous displacement boundary conditions at $x = 0$ are

$$\hat{u}_1(0) = \tilde{u}_2(0) = \tilde{u}_3(0) = 0, \tag{103}$$

while homogeneous traction boundary conditions at $x = 0$ are

$$-\hat{p}(0) + 2\mu\hat{u}_1'(0) = 0, \tag{104a}$$
$$\tilde{u}_2'(0) + k_y\,\hat{u}_1(0) = 0, \tag{104b}$$
$$\tilde{u}_3'(0) + k_z\,\hat{u}_1(0) = 0. \tag{104c}$$

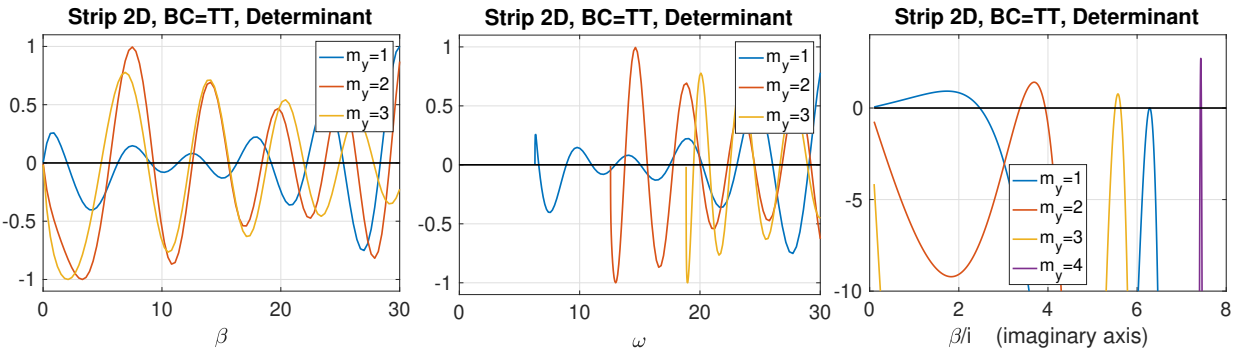

Figure 9: Plot of the determinant $\det(M_{\text{TT}})$ versus real β (left) and real ω (middle). Right: surface waves correspond to roots along imaginary β.

Similar boundary conditions can be found at $x = 1$. Substituting (99) into the displacement or traction boundary conditions at $x = 0$ and $x = 1$ leads to a homogeneous linear system of equations for six unknowns $[A_1, B_1, A_2, B_2, P_1, P_2]$ in three dimensions and four unknowns $[A_1, B_1, P_1, P_2]$ in two dimensions. For nontrivial solutions the matrix in the linear system must be singular, which leads to a determinant condition. The values of β (and corresponding values for ω) for which the determinant is zero provide the sought after eigenvalues. For example, in two dimensions ($m_z = 0$) with traction boundary conditions on both sides one is led to the matrix

$$M_{\text{TT}} \overset{\text{def}}{=} \begin{bmatrix} 0 & 2\mu\beta & \gamma_1 & \gamma_1 \\ -\beta^2 + k^2 & 0 & \gamma_2 & -\gamma_2 \\ \left(-\beta^2 + k^2\right)\cos\beta & \left(-\beta^2 + k^2\right)\sin\beta & \gamma_2 e^{k} & -\gamma_2 e^{-k} \\ -2\mu\beta\sin\beta & 2\mu\beta\cos\beta & \gamma_1 e^{k} & \gamma_1 e^{-k} \end{bmatrix}, \tag{105}$$

where

$$\gamma_1 = \frac{-\beta^2 + k^2}{\beta^2 + k^2}, \qquad \gamma_1 = \frac{2k^3}{\mu\left(\beta^2 + k^2\right)}. \tag{106}$$

The determinant reduces to

$$\det(M_{\text{TT}}) = R_1(\beta, k)\sin\beta\sinh k + R_2(\beta, k)(\cos\beta\cosh k - 1), \tag{107}$$

where

$$R_1 = -\frac{2\left(\beta^8 - 4\beta^6k^2 + 6\beta^4k^4 - 20\beta^2k^6 + k^8\right)}{\left(\beta^2 + k^2\right)^2}, \qquad R_2 = \frac{16k^3\beta\left(\beta^2 - k^2\right)^2}{\left(\beta^2 + k^2\right)^2}. \tag{108}$$

Note that determinant condition $\det(M_{\text{TT}}) = 0$ is independent of the material parameters ρ and μ. Thus the roots β are universal, and depend only on the wave number k. The values for ω, however,

do depend on c in view of the definition in (100b). In general, there are an infinite number of eigenvalues labeled by $m_x = 1, 2, 3, \ldots$ for a chosen wave-number pair $(k_y, k_z) = 2\pi\,(m_y, m_z)$.

Figure 9 graphs $\det(M_{\rm TT})$ versus real β and ω ($c = 1$) for a two-dimensional strip with different values of m_y. (The determinant is scaled independently for each m_y to clarify the graphs.) Eigenvalues correspond to the locations in β or ω where the determinant is zero, and these correspond to some of the entries for ω in Table 1. Figure 9 also graphs the imaginary part of the determinant versus imaginary β. Roots along the imaginary axis for β correspond to surface waves as discussed further below. Note that since ω must be real (from energy conservation), β^2 must also be real in view of (100b) and thus roots for β must lie along the real or imaginary axes. The eigenmodes can thus be grouped into two classes. The first class, called bulk modes, has $\beta^2 > 0$ in (100b). In this case $\beta \in \mathbb{R}$ and the displacements in (99) have sinusoidal dependence. The second class, called surface waves, corresponds to $\beta^2 < 0$ so that β is pure imaginary in which case $\cos(\beta x)$ and $\sin(\beta x)$ have an exponential behavior of cosh and sinh, respectively. It is found that surface waves can occur when there is a traction boundary condition, and these solutions are indicated in Table 1 by the modes with a superscript *star* as found for the BC = TD and TT.

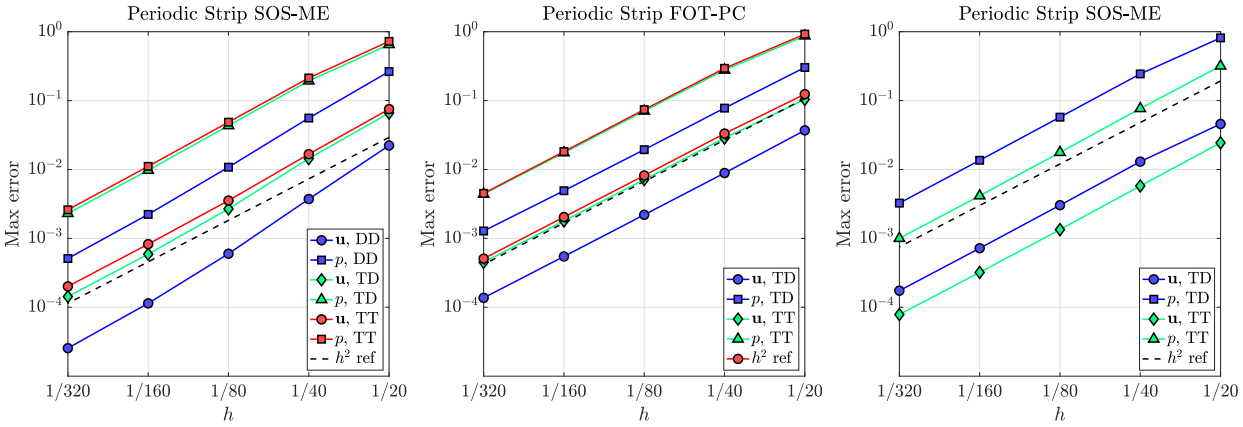

Figure 10: Solution convergence for a two-dimensional periodic channel. Left: SOS-ME scheme. Middle: FOT-PC scheme. Right: SOS-ME scheme results for a surface wave solution.

Selected eigenmode solutions are chosen with corresponding eigenvalues given in Table 1 for $c = 1$ to verify the stability and accuracy of the fractional-step methods. Three cases of boundary conditions are considered. There is a case with displacement boundary conditions on both sides, BC = DD. There is a case with traction boundary conditions on both sides, BC = TT. Finally there is a case with a traction condition on the left and displacement condition on the right, BC = DT.

Grid convergence results for the SOS-ME and FOT-PC schemes are given in Figure 10 for the two-dimensional channel with $m_z = 0$. The left and middle graphs show results at $t = 1.0$ for three BC cases. Solutions are computed to modes $\mathrm{DD}_{2,2}$ ($m_x = 2$, $m_y = 2$), $\mathrm{TD}_{3,3}$ and $\mathrm{TT}_{3,3}$ (see Table 1). The numerical solutions obtained from both fractional-step schemes are seen to converge at close to second-order accuracy, and we note that the maximum errors in the displacement and pressure are similar for the two schemes. Figure 10 also shows similar grid convergence results for the surface wave modes $\mathrm{TD}^*_{1,2}$ and $\mathrm{TT}^*_{2,3}$. The surface wave modes also converge at close to second-order accuracy.

Representative results from the two-dimensional computations are displayed in Figure 11. The top row shows results for BC = DD (bulk mode $\mathrm{DD}_{2,3}$ in Table 1), the middle row for BC = TT (surface-wave mode $\mathrm{TT}^*_{1,3}$ in Table 1), and the bottom row shows results for BC = TD (bulk mode $\mathrm{TD}_{3,2}$ in Table 1). The leftmost figures show the computed displacement applied to the grid

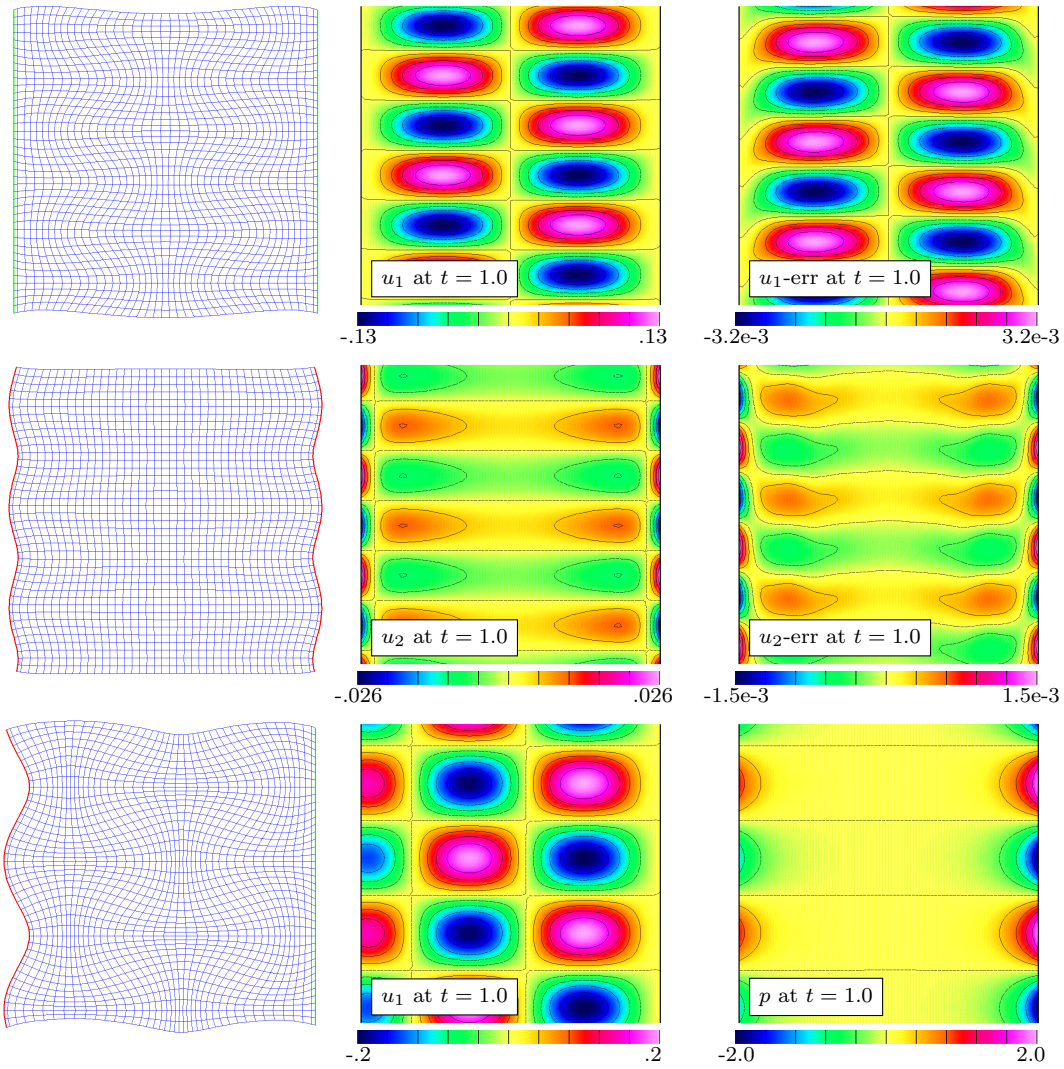

Figure 11: Computed results using the SOS-ME scheme for a two-dimensional periodic channel. Left column: grid displacement at selected times. Top: contours of u_1 and the error in u_1 for BCs = DD, bulk mode $\mathrm{DD}_{2,3}$. Middle: contours of u_2 and the error in u_2 for BCs = TT, surface-wave mode $\mathrm{TT}_{1,3}$. Bottom: contours of u_1 and p for BCs = TD, bulk mode $\mathrm{TD}_{3,2}$.

points, with a scaling chosen for illustrative purposes. The traction and displacement boundaries are clearly identified as the grid displacement is zero on the displacement boundaries. The top row shows contours of u_1 and the error in u_1. The solution in the middle row is a surface wave mode as can be seen in the contours of u_2 which are largest near the left and right boundaries. The bottom row shows a bulk mode as evident from the contours of u_1. Note that the pressure tends to be largest near boundaries, even for bulk modes. The errors are seen to be smooth and generally largest near the traction boundaries.

Since the upwind dissipation is a key component of the new schemes presented here, we now show what happens when the SOS-ME scheme is used for a problem with traction boundary conditions with the upwind dissipation turned off. Figure 12 shows computed solutions for the strip with BC = TD and with no upwind dissipation. The left plot shows the computed pressure at $t = 9$ using a grid with $\Delta x = 1/40$, while the right plot shows the computed pressure at $t = 4.5$ using a grid with $\Delta x = 1/80$. Note that the number of time steps taken is 567 for both results, and

Periodic Strip 2D, BC = DD	
BC_{m_x,m_y}	ω
$\mathrm{DD}_{1,1}$	7.646551296
$\mathrm{DD}_{2,1}$	10.25275587
$\mathrm{DD}_{3,1}$	13.17025759
$\mathrm{DD}_{4,1}$	16.17753257
$\mathrm{DD}_{1,2}$	13.10449553
$\mathrm{DD}_{2,2}$	14.55325034
$\mathrm{DD}_{3,2}$	16.60175273
$\mathrm{DD}_{4,2}$	19.00950205
$\mathrm{DD}_{1,3}$	19.17353069
$\mathrm{DD}_{2,3}$	20.10518332
$\mathrm{DD}_{3,3}$	21.54569844
$\mathrm{DD}_{4,3}$	23.38042985

Periodic Strip 2D, BC = TD	
BC_{m_x,m_y}	ω
$\mathrm{TD}^*_{1,1}$	6.104673313
$\mathrm{TD}_{2,1}$	8.287247575
$\mathrm{TD}_{3,1}$	10.69417027
$\mathrm{TD}_{4,1}$	13.04158614
$\mathrm{TD}^*_{1,2}$	12.00857399
$\mathrm{TD}_{2,2}$	13.37745529
$\mathrm{TD}_{3,2}$	15.0711901
$\mathrm{TD}_{4,2}$	17.19904633
$\mathrm{TD}^*_{1,3}$	18.0073517
$\mathrm{TD}_{2,3}$	19.29561695
$\mathrm{TD}_{3,3}$	20.42295669
$\mathrm{TD}_{4,3}$	22.01445954

Periodic Strip 2D, BC = TT	
BC_{m_x,m_y}	ω
$\mathrm{TT}^*_{1,1}$	5.776606091
$\mathrm{TT}_{2,1}$	6.600586854
$\mathrm{TT}_{3,1}$	8.885765876
$\mathrm{TT}_{4,1}$	11.00306926
$\mathrm{TT}^*_{1,2}$	11.93276623
$\mathrm{TT}^*_{2,2}$	12.10621807
$\mathrm{TT}_{3,2}$	13.75322319
$\mathrm{TT}_{4,2}$	15.62481284
$\mathrm{TT}^*_{1,3}$	17.98871518
$\mathrm{TT}^*_{2,3}$	18.02750111
$\mathrm{TT}_{3,3}$	19.47277875
$\mathrm{TT}_{4,3}$	20.79848883

Table 1: Selected eigenvalues ω for eigenmodes in a two-dimensional channel, periodic in the y direction with wave number $2\pi m_y$ and $c = 1$. Cases with BC = DD use displacement conditions at $x = 0$ and $x = 1$, while cases with BC = TT use traction boundary conditions at both ends. Cases with BC = TD use a traction condition at $x = 0$ and a displacement condition at $x = 1$. Surface waves are denoted with a superscript *star* as in $\mathrm{TT}^*_{1,1}$.

$\|p\|_\infty = 1081$ for the computed pressure on the left and $\|p\|_\infty = 1188$ for the computed pressure on the right. As expected, $\|p\|_\infty$ is approximately equal for both results since the growth of the unstable mode depends on the number of steps taken, rather than the final time. Interestingly, the unstable solution resembles a surface wave concentrated near the traction boundary with the solution decaying exponentially away from the boundary itself.

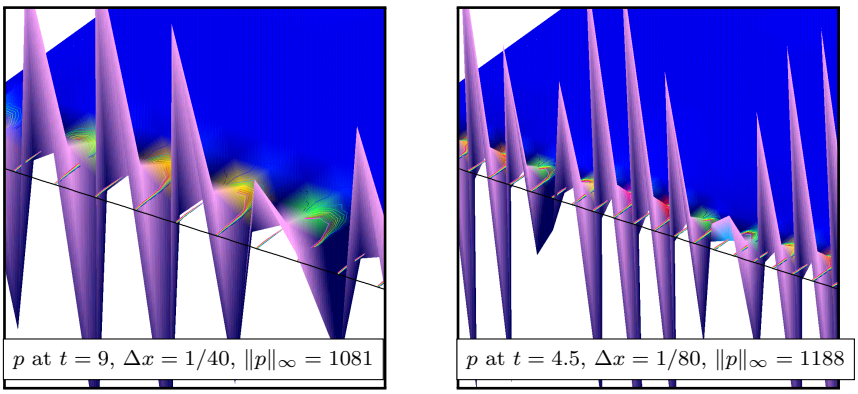

Figure 12: Unstable mode for a strip computed without upwind dissipation. Surface plots of pressure. Left: $\Delta x = 1/40$, 567 steps. Right: $\Delta x = 1/80$, 567 steps.

$\mathrm{BC}_{m_x,m_y,m_z}$	ω
$\mathrm{TT}_{4,1,1}$	10.76496763927843
$\mathrm{TD}^*_{1,1,1}$	8.51405494367735

Table 2: Selected eigenvalues ($c = 1$) for eigenmodes of a three-dimensional slab, periodic in the y and z directions, with with traction boundary conditions at $x = 0$ and $x = 1$ (BCs = TT) or with a traction condition at $x = 0$ and a displacement condition at $x = 1$ (BCs = TD).

Figure 13 shows results for some computations in three dimensions using the SOS-ME scheme. Grid convergence results show the errors as a function of the grid spacing. Results are shown for modes $\mathrm{TT}_{4,1,1}$ and $\mathrm{TD}^*_{1,1,1}$ with corresponding eigenvalues given in Table 2. The results confirm that the convergence rate is very close to second order. The right figure plots the x-component

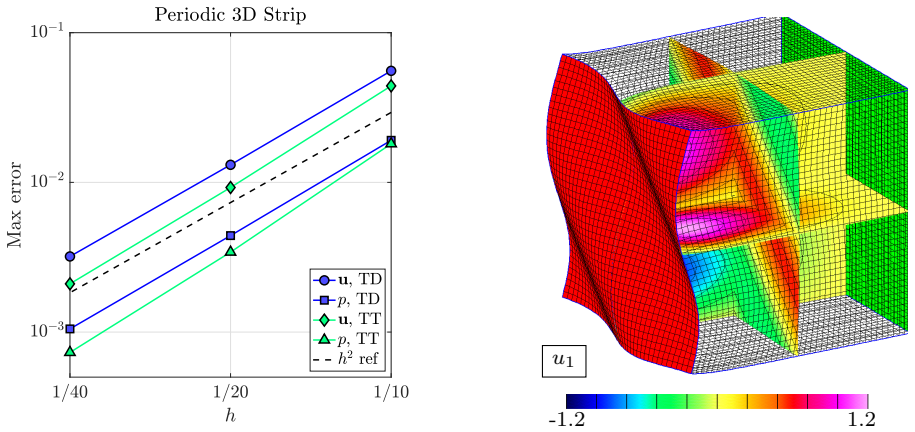

Figure 13: Computed results for the three-dimensional periodic channel using the SOS-ME scheme. Left: grid convergence. Right: displacement on surface and contour planes of u_1 for the TD boundary-condition pair.

of the displacement of the grid for a TD case. In particular, the deformation of the zero-traction boundary at $x = 0$ is shown. Selected contour planes plotting the displacement in the interior are also shown with the largest values appearing near the zero-traction boundary.

6.3. Eigenmodes in two-dimensional circular domains

Exact eigenmode solutions of the equations of incompressible linear elasticity for an annulus with inner radius r_a and outer radius r_b can be used to verify the fractional-step schemes for circular domains. In two-dimensional polar coordinates (r, θ) solutions take the form

$$\begin{bmatrix} \mathbf{u}(r,\theta,t) \\ p(r,\theta,t) \end{bmatrix} = \begin{bmatrix} \hat{\mathbf{u}}(r) \\ \hat{p}(r) \end{bmatrix} e^{im_\theta \theta}\, e^{i\omega t}, \tag{109}$$

where ω is a frequency and the integer m_θ determines the wave number in the circumferential direction. For a circular domain, it is convenient to express the displacement $\hat{\mathbf{u}}(r)$ in terms of a radial displacement $\hat{u}_r(r)$ and a circumferential displacement $\hat{u}_\theta(r) = i\tilde{u}_\theta(r)$. The radial component of displacement and the pressure have the form

$$\hat{u}_r(r) = \frac{1}{r}\left(A_1 J_{m_\theta}\left(\frac{\omega r}{c}\right) + B_1 Y_{m_\theta}\left(\frac{\omega r}{c}\right)\right) + \frac{1}{\rho\,\omega^2}\hat{p}'(r), \tag{110a}$$

$$\hat{p}(r) = P_1 r^{m_\theta} + P_2 r^{-m_\theta}, \tag{110b}$$

where J_{m_θ} and Y_{m_θ} are Bessel functions of the first and second kinds, respectively, and (A_1, B_1, P_1, P_2) are constants. The zero-divergence conditions gives the circumferential component of displacement in terms of the radial component as

$$\tilde{u}_\theta(r) = \frac{1}{m_\theta}\big(r\hat{u}_r(r)\big)', \tag{111}$$

assuming $m_\theta \neq 0$. Zero-displacement conditions on $r = r_s$, $s = a$ or b, are

$$\hat{u}_r(r_s) = \tilde{u}_\theta(r_s) = 0, \tag{112}$$

while zero-traction conditions are

$$-\hat{p}(r_s) + 2\mu\hat{u}_r'(r_s) = 0, \tag{113a}$$

$$\tilde{u}_\theta'(r_s) - \frac{1}{r_s}\big(\tilde{u}_\theta(r_s) - m_\theta\hat{u}_r(r_s)\big) = 0. \tag{113b}$$

Substituting (110) into the zero-displacement or zero-traction conditions at the inner and outer boundaries leads to a homogeneous linear system for the unknowns $[A_1, B_1, P_1, P_2]$. Setting the determinant of the associated matrix to zero leads to a transcendental equation for ω. For each value of m_θ, there are an infinite number of roots for ω, enumerated by $m_r = 1, 2, 3, \ldots$.

Selected eigenvalues are given in Table 3 for the three cases of boundary conditions, BC = TT (both zero-traction boundaries), BC = TD (inner boundary traction and outer boundary displacement) and BC = DD (both zero-displacement boundaries). The values in the table are computed using $r_a = 0.5$, $r_b = 1$, $\rho = 1$ and $\mu = 1$.

Annulus, BC = DD	
$\mathrm{BC}_{m_r,m_\theta}$	ω
$\mathrm{DD}_{1,1}$	12.51052065
$\mathrm{DD}_{2,1}$	17.9851201
$\mathrm{DD}_{3,1}$	25.1046496
$\mathrm{DD}_{4,1}$	30.9077106
$\mathrm{DD}_{1,2}$	12.33452228
$\mathrm{DD}_{2,2}$	18.03546757
$\mathrm{DD}_{3,2}$	25.01975289
$\mathrm{DD}_{4,2}$	30.93707184
$\mathrm{DD}_{1,3}$	12.17699978
$\mathrm{DD}_{2,3}$	18.13308903
$\mathrm{DD}_{3,3}$	24.94974373
$\mathrm{DD}_{4,3}$	30.99381855

Annulus, BC = TD	
$\mathrm{BC}_{m_r,m_\theta}$	ω
$\mathrm{TD}_{1,1}$	5.930113702
$\mathrm{TD}_{2,1}$	10.04122887
$\mathrm{TD}_{3,1}$	16.22223625
$\mathrm{TD}_{4,1}$	22.26179962
$\mathrm{TD}_{1,2}$	7.320927074
$\mathrm{TD}_{2,2}$	10.78830876
$\mathrm{TD}_{3,2}$	16.57611517
$\mathrm{TD}_{4,2}$	22.31295973
$\mathrm{TD}_{1,3}$	7.614801451
$\mathrm{TD}_{2,3}$	12.34788623
$\mathrm{TD}_{3,3}$	17.32195472
$\mathrm{TD}_{4,3}$	22.62154602

Annulus, BC = TT	
$\mathrm{BC}_{m_r,m_\theta}$	ω
$\mathrm{TT}_{1,1}$	3.434667449
$\mathrm{TT}_{2,1}$	7.74079964
$\mathrm{TT}_{3,1}$	13.00938974
$\mathrm{TT}_{4,1}$	19.13885532
$\mathrm{TT}_{1,2}$	4.796411934
$\mathrm{TT}_{2,2}$	9.402245191
$\mathrm{TT}_{3,2}$	13.62238307
$\mathrm{TT}_{4,2}$	19.44672755
$\mathrm{TT}_{1,3}$	2.543959252
$\mathrm{TT}_{2,3}$	6.294831953
$\mathrm{TT}_{3,3}$	10.67437429
$\mathrm{TT}_{4,3}$	14.84146791

Table 3: Selected eigenvalues for eigenmodes of an annulus for BC = DD, BC = TD and BC = TT assuming $r_a = 0.5$, $r_b = 1$, $\rho = 1$ and $\mu = 1$.

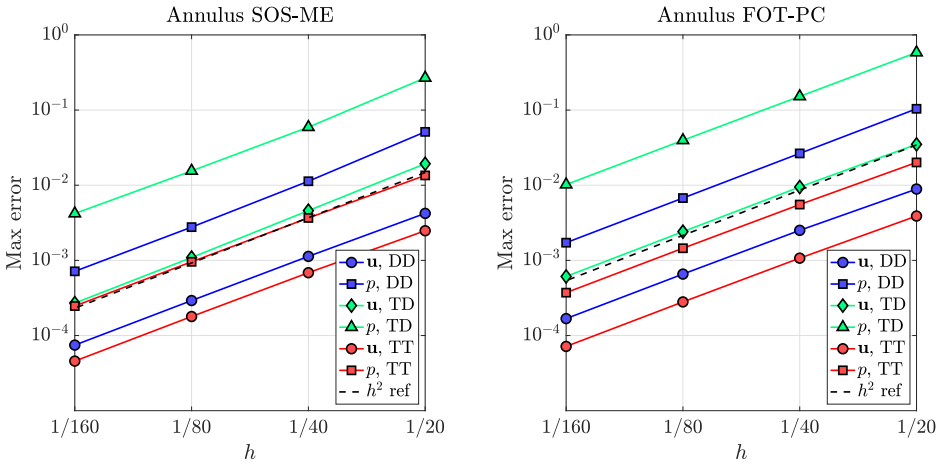

Figure 14: Grid convergence for an eigenfunction of an annulus. Left: SOS-ME-scheme at $t = 1.0$. Right: FOT-PC-scheme at $t = 1.0$. Modes $\mathrm{DD}_{1,1}$, $\mathrm{TD}_{4,2}$, and $\mathrm{TT}_{2,3}$.

Grid convergence results for the annulus for the SOS-ME and FOT-PC schemes are given in Figure 14. Results are shown for the three different BC cases for modes $\mathrm{DD}_{1,1}$, $\mathrm{TD}_{4,2}$, and $\mathrm{TT}_{2,3}$ (see Table 3). Both schemes are seen to converge at close to second-order accuracy for the displacements and pressure in the max-norm. The errors in the two time-stepping schemes are roughly the same with the SOS-ME scheme being slightly more accurate in general.

Figure 15 shows the form of the annulus solution for three different cases. The top row shows results for mode $\mathrm{DD}_{1,1}$, the middle row for mode $\mathrm{TD}_{1,1}$ and the bottom row for mode $\mathrm{TT}_{1,1}$. The leftmost figures show the displacement of the grid points, with some arbitrary scaling. The traction

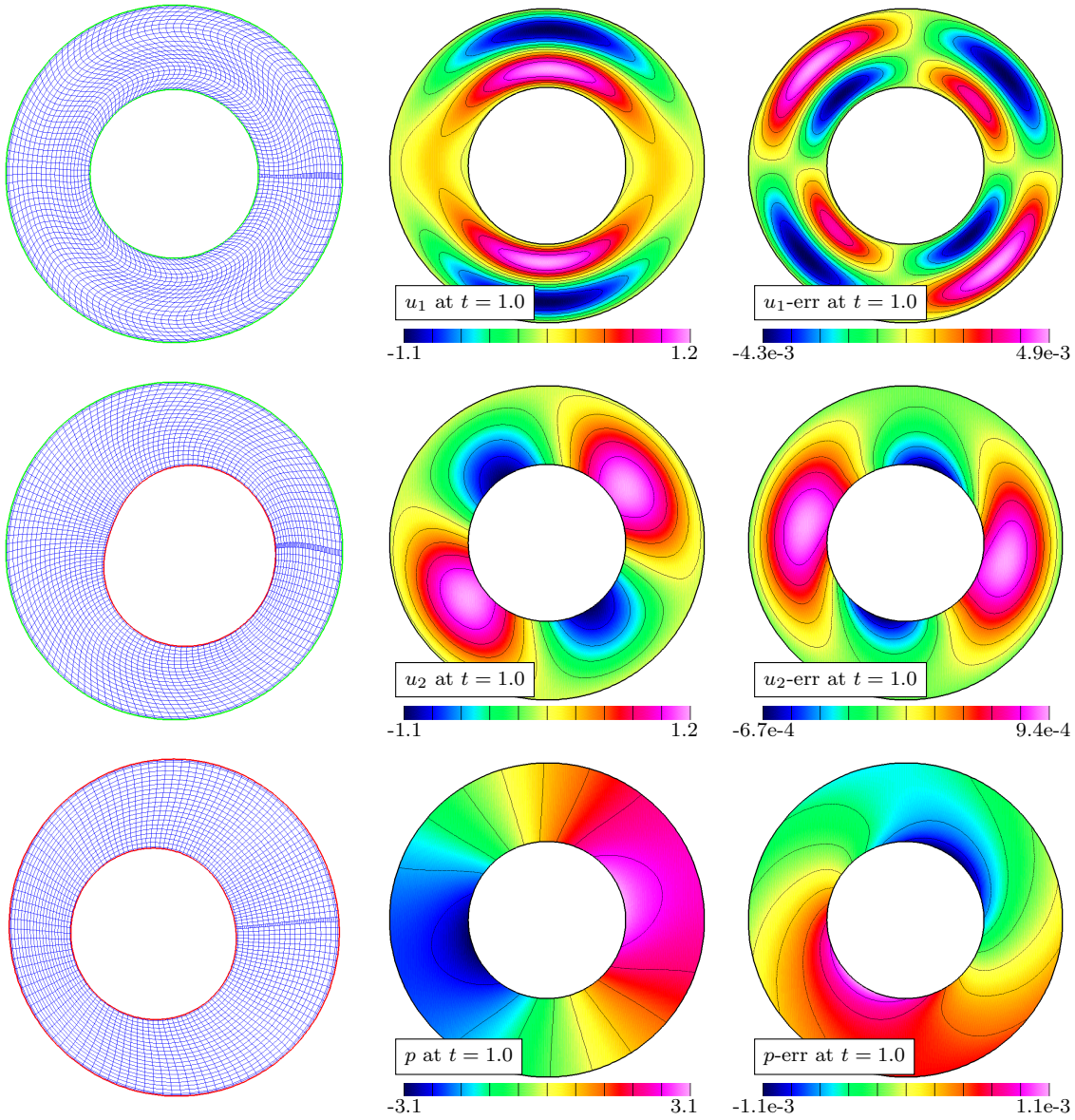

Figure 15: Exact solution for an annulus. Top row: mode $\mathrm{DD}_{1,1}$. Middle row: mode $\mathrm{TD}_{1,1}$. Bottom row: mode $\mathrm{TT}_{1,1}$.

and displacement boundaries are clearly identified as the grid displacement is zero on the latter boundaries. The middle and right figures show contours of selected components of the solution and corresponding errors. The errors are seen to be smooth.

In the limit $r_a \to 0$, the problem domain becomes a solid disk of radius r_b. Eigenmode solutions have the form in (110), but with $B_1 = 0$ and $P_2 = 0$ so that the singularity in the solution at $r = 0$ is removed. The reduced form of the solution is substituted into the boundary conditions at $r = r_b$, either the zero-displacement or zero-traction conditions, resulting in an eigenvalue problem for ω for a chosen $m_\theta \neq 0$. Selected values are given in Table 4 for displacement and traction boundary conditions assuming $\rho = 1$, $\mu = 1$ and $r_b = 1$.

The composite grid for the disk geometry, denoted by $\mathcal{G}_d^{(j)}$, consist of two component grids, each with grid spacing chosen to approximately equal $\Delta s^{(j)} = 1/(10j)$. A thin annular grid lies next to the boundary of the disk. A background Cartesian grid covers the interior of the domain and

Disk, Displacement BC	
$\mathrm{BC}_{m_r,m_\theta}$	ω
$\mathrm{D}_{1,1}$	5.135622302
$\mathrm{D}_{2,1}$	8.41724414
$\mathrm{D}_{3,1}$	11.61984117
$\mathrm{D}_{4,1}$	14.79595178
$\mathrm{D}_{1,2}$	6.380161896
$\mathrm{D}_{2,2}$	9.76102313
$\mathrm{D}_{3,2}$	13.01520072
$\mathrm{D}_{4,2}$	16.22346616
$\mathrm{D}_{1,3}$	7.588342435
$\mathrm{D}_{2,3}$	11.06470949
$\mathrm{D}_{3,3}$	14.37253667
$\mathrm{D}_{4,3}$	17.61596605

Disk, Traction BC	
$\mathrm{BC}_{m_r,m_\theta}$	ω
$\mathrm{T}_{1,1}$	3.054236928
$\mathrm{T}_{2,1}$	6.706133194
$\mathrm{T}_{3,1}$	9.969467823
$\mathrm{T}_{4,1}$	13.17037086
$\mathrm{T}_{1,2}$	2.353887635
$\mathrm{T}_{2,2}$	4.78444428
$\mathrm{T}_{3,2}$	8.176670243
$\mathrm{T}_{4,2}$	11.44602944
$\mathrm{T}_{1,3}$	3.64712633
$\mathrm{T}_{2,3}$	6.478105792
$\mathrm{T}_{3,3}$	9.619790598
$\mathrm{T}_{4,3}$	12.88225844

Table 4: Selected eigenvalues for eigenmodes of a disk for BC = D and BC = T using $r_b = 1$, $\rho = 1$ and $\mu = 1$.

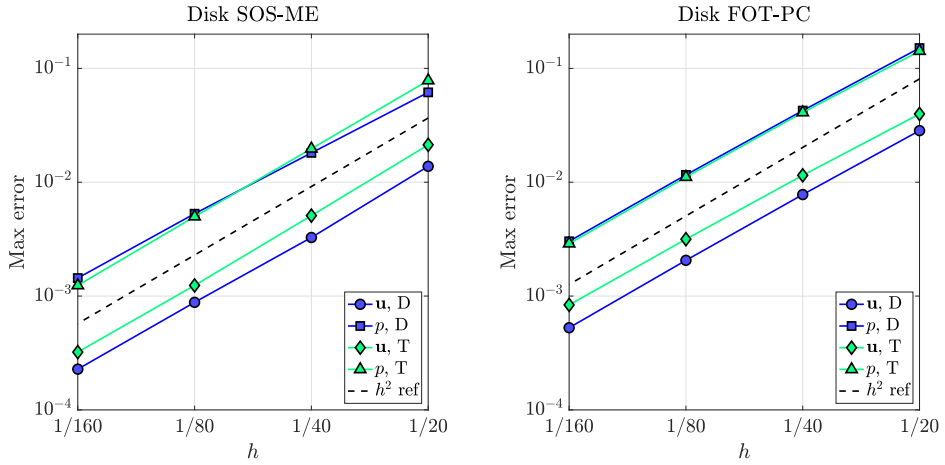

Figure 16: Grid convergence for an eigenfunction of a disk. Left: SOS-ME-scheme at $t = 1.0$. Right: FOT-PC-scheme at $t = 1.0$. Modes $D_{2,1}$ and $T_{3,2}$.

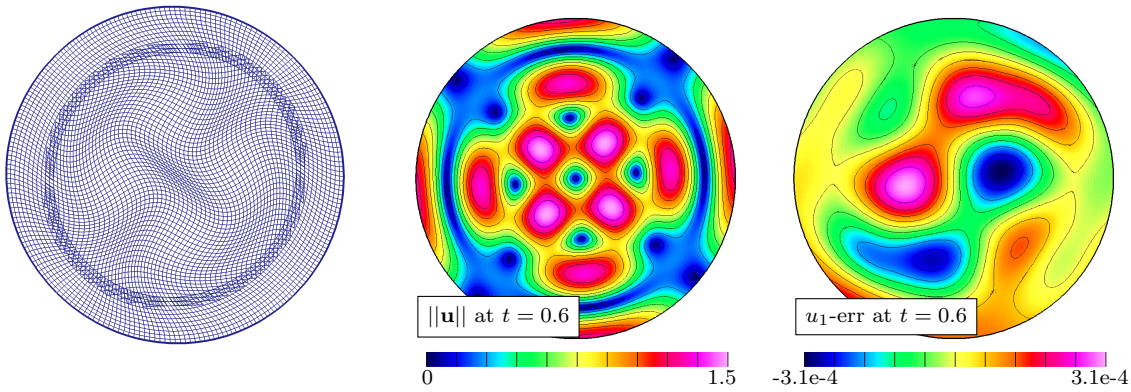

Figure 17: Eigenmode $\mathrm{T}_{3,2}$ of a disk. Computed solution for traction boundary conditions. Left: displacement on the grid $\mathcal{G}^{(4)}$. Middle: contours of the displacement norm $\|\mathbf{u}\|$. Right: contours of the error in u_1.

removes the polar singularity in the annular grid had it been extended to $r = 0$.

Grid convergence results for the disk using the SOS-ME and FOT-PC schemes are given in Figure 16. Results are shown for mode $D_{2,1}$ using a zero-displacement condition at $r = r_b$, and for mode $T_{3,2}$ using a zero-traction condition. Both schemes are seen to converge at close to second-

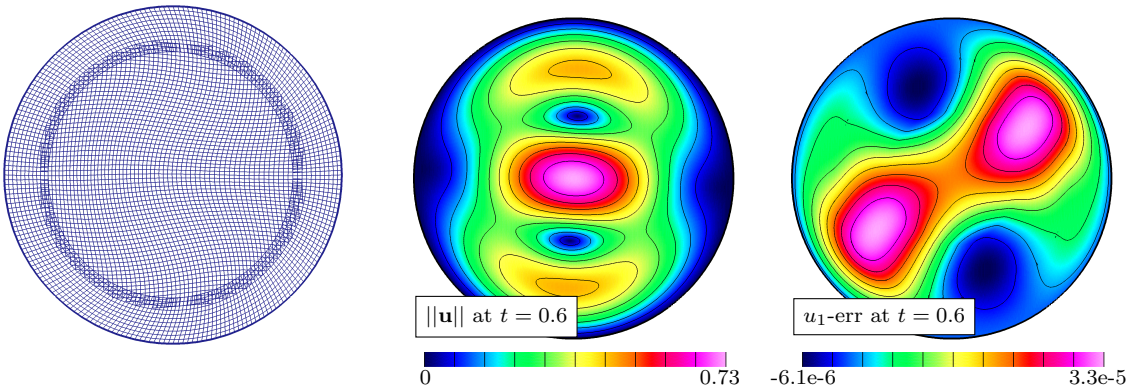

Figure 18: Eigenmode $\mathrm{D}_{1,2}$ of a disk. Computed solution for displacement boundary conditions. Left: displacement on the grid $\mathcal{G}^{(4)}$. Middle: contours of the displacement norm $\|\mathbf{u}\|$. Right: contours of the error in u_1.

order accuracy in the max-norm for both the displacements and the pressure. The errors in the SOS-ME scheme are generally slightly smaller than those from the FOT-PC scheme. The plots in Figures 17 and 18 show the behavior of the computed solutions for $\mathrm{T}_{3,2}$ and $\mathrm{D}_{1,2}$, respectively. The displacement of the grid points are shown on the leftmost plots of both figures. Contours of the norm of the displacement, $\|\mathbf{u}\|$, are shown in the middle plots, while the errors in u_1 are shown on the right. The contour lines of $\|\mathbf{u}\|$ are seen to pass smoothly across the interpolation boundary. The errors in u_1 are smooth and only close examination shows where the contour lines cross the interpolation boundary between the component grids.

Figure 19 shows the computed solution on a disk with traction boundary conditions for mode $\mathrm{T}_{51,1}$. This mode with $m_\theta = 51$ and $m_r = 1$ represents a surface wave that is concentrated in a boundary layer near the outer radius of the disk. The surface wave primarily propagates in the circumferential direction and its angular phase speed is estimated to be slightly less than one.

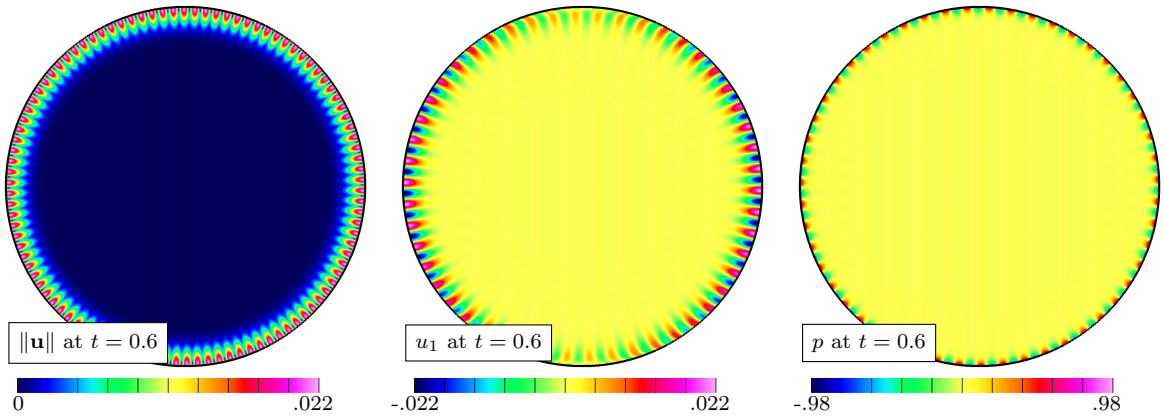

Figure 19: Eigenmode $\mathrm{T}_{51,1}$ of a disk with traction boundary conditions representing a surface-wave mode.

6.4. Vibrational modes of hollow and solid cylinders

In this section, vibrational modes in a hollow and solid cylinder are considered. In cylindrical coordinates (r, θ, z), the hollow cylinder has inner radius $r_a = 0.5$, outer radius $r_b = 1$ and axial length $\ell_z = 1$. The solid cylinder has an outer radius $r_b = 0.5$ and an axial length $\ell_z = 1$, with the inner radius r_a taken to be zero. Eigenmode solutions for the displacement vector and pressure

have the form

$$\begin{bmatrix}\mathbf{u}(r,\theta,z,t)\\ p(r,\theta,z,t)\end{bmatrix} = \begin{bmatrix}\hat{\mathbf{u}}(r)\\ \hat{p}(r)\end{bmatrix} e^{im_\theta\theta}\, e^{ik_z z}\, e^{i\omega t}, \tag{114}$$

where ω is a frequency, m_θ determines the circumferential mode (as before), and $k_z = 2\pi m_z \ell_z = 2\pi m_z$ for an integer m_z gives the wave number in the axial direction. Solutions for $\hat{\mathbf{u}}(r) = (\hat{u}_r, \hat{u}_\theta, \hat{u}_z)^T = (\hat{u}_r, i\tilde{u}_\theta, i\tilde{u}_z)^T$ and $\hat{p}(r)$ have the form

$$\hat{u}_r(r) = \frac{1}{2}\big(\hat{u}_s(r) + \hat{u}_d(r)\big), \tag{115a}$$

$$\tilde{u}_\theta(r) = \frac{1}{2}\big(\hat{u}_s(r) - \hat{u}_d(r)\big), \tag{115b}$$

$$\hat{p}(r) = A_p I_{m_\theta}(k_z r) + B_p K_{m_\theta}(k_z r), \tag{115c}$$

where $\hat{u}_s$ and $\hat{u}_d$ are the sum and difference of the displacements in the radial and circumferential directions, and they are given by

$$\hat{u}_s(r) = A_s J_{m_\theta-1}(\beta r) + B_s Y_{m_\theta-1}(\beta r) + \frac{k_z}{\mu(\beta^2+k_z^2)}\big(A_p I_{m_\theta-1}(k_z r) - B_p K_{m_\theta-1}(k_z r)\big), \tag{115d}$$

$$\hat{u}_d(r) = A_d J_{m_\theta+1}(\beta r) + B_d Y_{m_\theta+1}(\beta r) + \frac{k_z}{\mu(\beta^2+k_z^2)}\big(A_p I_{m_\theta+1}(k_z r) - B_p K_{m_\theta+1}(k_z r)\big). \tag{115e}$$

Here, $(A_s, B_s, A_d, B_d, A_p, B_p)$ are constants, I_{m_θ} and K_{m_θ} are modified Bessel functions of the first and second kinds, respectively, and β is now specified by

$$\beta^2 = \frac{\omega^2}{c^2} - k_z^2. \tag{116}$$

The zero-divergence condition determines the axial component of displacement as

$$\tilde{u}_z(r) = \frac{1}{k_z}\left(\hat{u}_r'(r) + \frac{1}{r}\hat{u}_r(r) - \frac{m_\theta}{r}\tilde{u}_\theta(r)\right), \tag{117}$$

assuming $k_z \neq 0$. Zero-displacement conditions at $r = r_s$, $s = a$ or b, are

$$\hat{u}_r(r_s) = \tilde{u}_\theta(r_s) = \tilde{u}_z(r_s) = 0, \tag{118}$$

while zero-traction conditions become

$$-\hat{p}(r_s) + 2\mu\hat{u}_r'(r_s) = 0, \tag{119a}$$

$$\tilde{u}_\theta'(r_s) - \frac{1}{r_s}\big(\tilde{u}_\theta(r_s) - m_\theta\hat{u}_r(r_s)\big) = 0, \tag{119b}$$

$$\tilde{u}_z'(r_s) + k_z\hat{u}_r(r_s) = 0. \tag{119c}$$

Substituting the components of the solution into the zero-displacement or zero-traction conditions leads to an eigenvalue problem for chosen integer values for m_θ and m_z. For the case of the hollow cylinder, boundary conditions are applied at $r = r_a$ and r_b which results in a homogeneous linear system of equations for six unknowns $[A_d, B_d, A_s, B_s, A_p, B_p]$. The eigenvalues ω are roots of a determinant condition, and these values are given in Table 5 for selected eigenmodes, indexed by $m_r = 1, 2, \ldots$. Note that surface-wave solutions for which $\beta^2 < 0$ can be found the traction-traction (TT) case, and two of these eigenmode solutions are indicated with a star superscript as before.

Hollow Cylinder, BC = DD	
$\text{BC}_{m_r,m_\theta,m_z}$	ω
$\text{DD}_{1,1,1}$	9.049757526
$\text{DD}_{2,1,1}$	12.34088555
$\text{DD}_{1,2,1}$	9.307949709
$\text{DD}_{2,2,1}$	12.43448769

Hollow Cylinder, BC = TD	
$\text{BC}_{m_r,m_\theta,m_z}$	ω
$\text{TD}_{1,1,1}$	7.564862354
$\text{TD}_{2,1,1}$	8.191643356
$\text{TD}_{1,2,1}$	7.642573629
$\text{TD}_{2,2,1}$	8.737850269

Hollow Cylinder, BC = TT	
$\text{BC}_{m_r,m_\theta,m_z}$	ω
$\text{TT}^*_{1,1,1}$	5.510195493
$\text{TT}_{2,1,1}$	6.482729599
$\text{TT}^*_{1,2,1}$	5.700236897
$\text{TT}_{2,2,1}$	6.964881755

Table 5: Selected eigenvalues for eigenmodes of a hollow cylinder for BC = DD, TD and TT assuming $r_a = 0.5$, $r_b = 1$, $\ell_z = 1$, $\rho = 1$ and $\mu = 1$.

Solid Cylinder, BC = D	
$\text{BC}_{m_r,m_\theta,m_z}$	ω
$\text{D}_{1,1,1}$	8.651826352
$\text{D}_{2,1,1}$	12.22373030
$\text{D}_{1,2,1}$	11.17225940
$\text{D}_{2,2,1}$	14.41489412

Solid Cylinder, BC = T	
$\text{BC}_{m_r,m_\theta,m_z}$	ω
$\text{T}_{1,1,1}$	8.049235864
$\text{T}_{2,1,1}$	9.861543053
$\text{T}_{1,2,1}$	6.835992623
$\text{T}_{2,2,1}$	9.583744806

Table 6: Selected eigenvalues for eigenmodes of a solid cylinder for BC = D and T assuming $r_b = 0.5$, $\ell_z = 1$, $\rho = 1$ and $\mu = 1$.

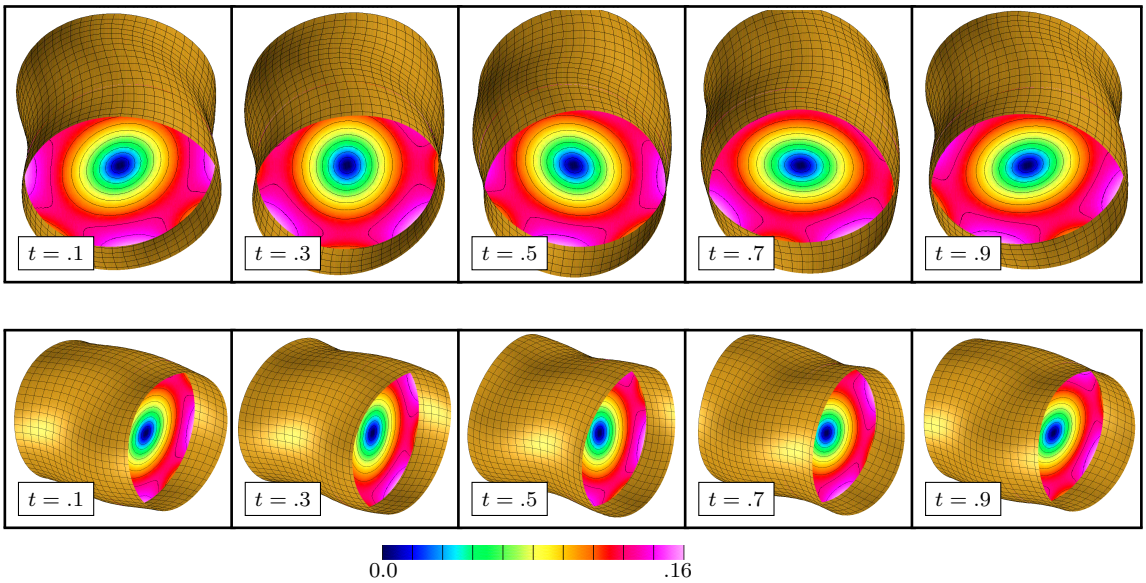

Figure 20: Vibrational mode of a solid cylinder with a traction boundary condition. Displacement of the cylinder surface and a contour plane of the displacement norm $\|\mathbf{u}\|$. Results are plotted at selected times for View 1 (top row) and View 2 (bottom row).

For the case of a solid cylinder, $r_a \to 0$ and B_d, B_s and B_p are set to zero to remove the singularity in the general solution at $r = 0$. Zero-displacement or zero-traction conditions are then applied at $r = r_b$, which leads to a homogeneous linear system of equations for three unknowns $[A_d, A_s, A_p]$. Again, there is a determinant condition for nontrivial solutions, and the roots are the eigenvalues. Table 6 gives values of ω for selected eigenmodes.

Figure 20 shows a representative computed eigenmode solution, $\text{T}_{1,2,1}$, at selected times for the case of a solid cylinder with traction boundary conditions. The solution is computed using a composite grid for the solid cylinder, denoted by $\mathcal{G}_c^{(j)}$, consisting of two component grids, each with grid spacings approximately equal to $\Delta s^{(j)} = 1/(10j)$ in all directions. One component grid is a narrow boundary-fitted cylindrical shell, while the other component grid is a background Cartesian grid covering the interior of the cylindrical domain. The displacement of the surface of the solid

cylinder is shown in the figure together with contours of the displacement norm $\|\mathbf{u}\|$ on a chosen cutting plane through the interior. The largest displacements for this vibrational mode generally occur near the surface of the cylinder with the core being nearly stationary. A wave appears to propagate along the axial direction of the cylinder and also rotate about the same axis. Figure 21 displays max-norm errors from a grid convergence study for both a hollow and a solid cylinder. The results show convergence rates close to second-order accuracy.

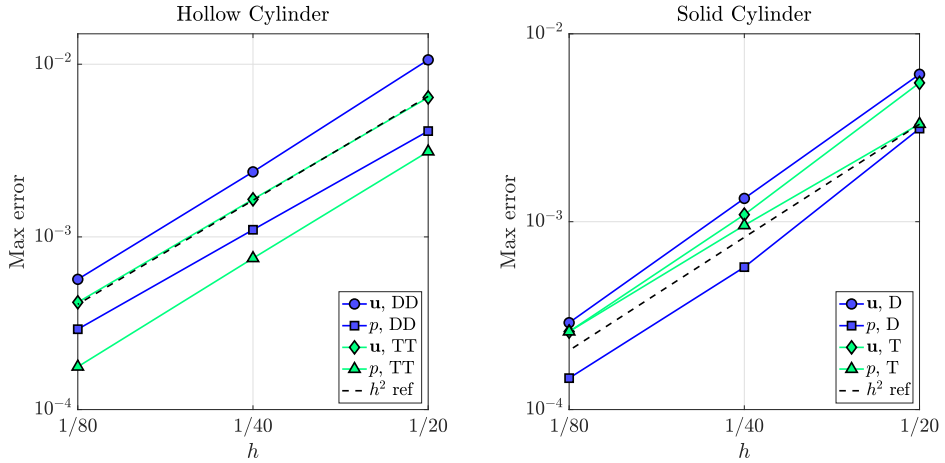

Figure 21: Grid convergence for eigenfunctions of a hollow cylinder (left) for the $\mathrm{DD}_{1,1,1}$ and $\mathrm{TT}^*_{1,1,1}$ modes, and of a solid cylinder (right) for the $\mathrm{D}_{1,2,1}$ and $\mathrm{T}_{1,2,1}$ modes. Solutions computed using the SOS-ME scheme at $t = 0.5$.

6.5. Vibrational modes of a incompressible solid sphere

We consider vibrational modes of a solid incompressible elastic sphere of radius $r = r_b$. Exact solutions can be found following the discussion in Love [37][8]. Let

$$\begin{bmatrix} \mathbf{u}(\mathbf{x},t) \\ p(\mathbf{x},t) \end{bmatrix} = \begin{bmatrix} \hat{\mathbf{u}}(\mathbf{x}) \\ \hat{p}(\mathbf{x}) \end{bmatrix} e^{i\omega t}, \tag{120}$$

where ω is the frequency of vibration as before. We consider solutions for the displacement $\hat{\mathbf{u}}(\mathbf{x}) = (\hat{u}_1, \hat{u}_2, \hat{u}_3)^T$ and the pressure $\hat{p}(\mathbf{x})$ of the form

$$\hat{u}_j(\mathbf{x}) = \psi_{m_\phi - 1}(kr)\partial_{x_j}\phi^{m_\theta}_{m_\phi}(\mathbf{x}) - \frac{m_\phi}{m_\phi + 1}\psi_{m_\phi+1}(kr)k^2 r^{2m_\phi+3}\partial_{x_j}\left[\frac{\phi^{m_\theta}_{m_\phi}(\mathbf{x})}{r^{2m_\phi+1}}\right] + \frac{1}{\rho\omega^2}\partial_{x_j}\hat{p}(\mathbf{x}), \tag{121a}$$

$$\hat{p}(\mathbf{x}) = \Omega^{m_\theta}_{m_\phi}(\mathbf{x}), \tag{121b}$$

where $k = \omega/c$ is a wave number, $r = \|\mathbf{x}\|$ is the radius, and

$$\psi_{m_\phi}(\eta) \stackrel{\text{def}}{=} \left(\frac{1}{\eta}\frac{d}{d\eta}\right)^{m_\phi}\left(\frac{\sin\eta}{\eta}\right), \tag{122}$$

is related to a spherical Bessel function of degree m_ϕ. The components of displacement and the pressure in (121) involve spherical (solid) harmonics $\phi^{m_\theta}_{m_\phi}(\mathbf{x})$ and $\Omega^{m_\theta}_{m_\phi}(\mathbf{x})$ both of integer degree m_ϕ

[8]The solutions discussed in Love [37] for a vibrating sphere are separated into two classes, and the ones considered here belong to the second class for which the gradient of the pressure is nonzero.

and integer order m_θ. In terms of spherical polar coordinates (r, θ, φ), these spherical harmonics are taken to be

$$\phi_{m_\phi}^{m_\theta}(\mathbf{x}) = A_u r^{m_\phi} P_{m_\phi}^{m_\theta}(\cos\varphi)\, e^{im_\theta\theta}, \tag{123a}$$

$$\Omega_{m_\phi}^{m_\theta}(\mathbf{x}) = A_p r^{m_\phi} P_{m_\phi}^{m_\theta}(\cos\varphi)\, e^{im_\theta\theta}, \tag{123b}$$

where $P_{m_\phi}^{m_\theta}(z)$ is an associated Legendre function[9] for degree $m_\phi = 0, 1, \ldots$ and order $m_\theta = -m_\phi, -m_\phi + 1, \ldots, m_\phi$, and (A_u, A_p) are constants to be determined.

Application of zero-displacement or zero-traction boundary conditions at $r = r_b$ leads to an eigenvalue problem for ω in terms of chosen integer values for m_ϕ and m_θ. There are infinitely many eigenvalues for each pair (m_ϕ, m_θ) and these are enumerated with $m_r = 1, 2, 3, \ldots$. For the case of a zero-displacement condition, an application of the analysis in [37] results in the determinant condition

$$\mathcal{D}_d(\eta) \stackrel{\text{def}}{=} \psi_{m_\phi+1}(\eta) = 0. \tag{124}$$

Roots $\eta = kr_b$ of (124) imply the eigenvalues, $\omega = \eta c/r_b$, and then for each root the constants (A_u, A_p) can be chosen to satisfy

$$A_p + \mu k^2 \psi_{m_\phi-1}(kr_b) A_u = 0. \tag{125}$$

For the case of zero-traction conditions, eigenvalues are obtained from roots of the determinant condition given by

$$\begin{aligned}\mathcal{D}_\tau(\eta) \stackrel{\text{def}}{=}\ & \frac{1}{2m_\phi+1}\left(\eta^2\psi_{m_\phi}(\eta) + 2(m_\phi-1)\psi_{m_\phi-1}(\eta)\right) \\ & + \frac{m_\phi}{m_\phi+1}\left(\frac{\eta^2}{2m_\phi+1} - 2(m_\phi-1)\right)\left(\psi_{m_\phi}(\eta) + \frac{2(m_\phi+2)}{\eta}\psi'_{m_\phi}(\eta)\right) = 0,\end{aligned} \tag{126}$$

and then the corresponding constants are chosen to satisfy

$$A_p + \mu k^2 \frac{m_\phi(2m_\phi+1)}{m_\phi+1}\left(\psi_{m_\phi}(kr_b) + \frac{2(m_\phi+2)}{kr_b}\psi'_{m_\phi}(kr_b)\right) A_u = 0. \tag{127}$$

Table 7 provides some selected eigenvalues and corresponding values for A_p in (123) for $\rho = \mu = 1$ and $r_b = 1$ assuming A_u is normalized to one.

Vibrational Modes of a Solid Sphere		
$\mathrm{BC}_{m_r,m_\phi,m_\theta}$	ω	A_p
$\mathrm{T}_{1,2,2}$	2.665622189	0.2775133580
$\mathrm{T}_{2,2,2}$	5.473039812	0.7875180276
$\mathrm{D}_{1,2,2}$	6.987932001	−0.6690671509
$\mathrm{D}_{2,2,2}$	10.41711855	0.4663534925

Table 7: Selected eigenvalues for vibrational modes of a solid sphere for $\rho = \mu = 1$ and $r_b = 1$, with traction (T) and displacement (D) boundary conditions.

The composite grids for the solid sphere, denoted by $\mathcal{G}_s^{(j)}$, consist of four component grids, each with grid spacing approximately equal to $\Delta s^{(j)} = 1/(10j)$. The sphere is covered with three

[9]The associated Legendre function $P_{m_\phi}^{m_\theta}(z)$ with $z = \cos\varphi$ is a polynomial in $\cos\varphi$ and $\sin\varphi$ of degree m_ϕ. Also note that $P_{m_\phi}^{-m_\theta}$ is a constant times $P_{m_\phi}^{m_\theta}$.

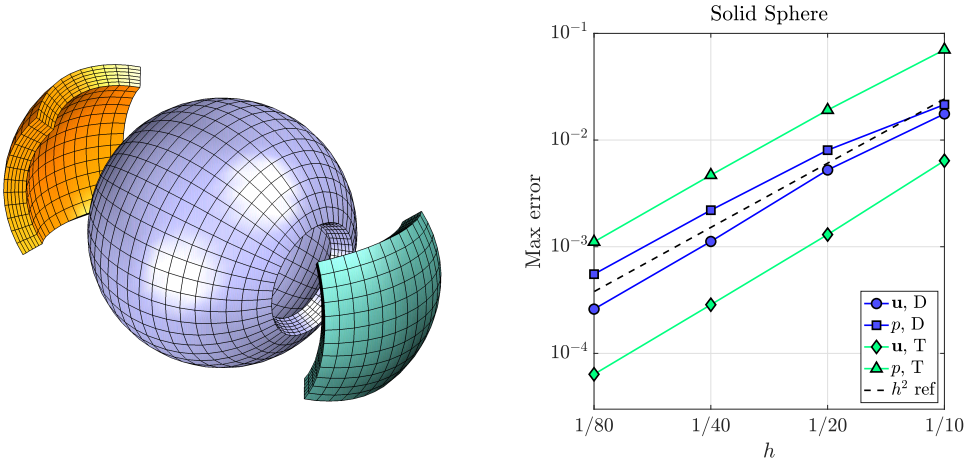

Figure 22: Left: exploded view of the surface patches of the overset grid for the interior of a sphere. Right: grid convergence for vibrational modes $T_{2,2,2}$ and $D_{1,2,2}$ of a solid sphere using the SOS-ME scheme at $t = 0.5$.

boundary-fitted patches near the surface as shown on the left in Figure 22. There is one patch specified using spherical polar coordinates that covers much of the sphere except near the poles. To remove the polar singularities there are two patches that cover the north and south poles, defined by orthographic mappings. A background Cartesian grid covers the interior of the sphere. The graph on the right of Figure 22 shows grid convergence results for two vibrational modes with traction and displacement boundary conditions, respectively. The traction case is mode $T_{2,2,2}$ in Table 7 while the displacement case is $D_{1,2,2}$. The results show that the solutions for the displacement and pressure are converging at close to second-order accuracy in the max-norm.

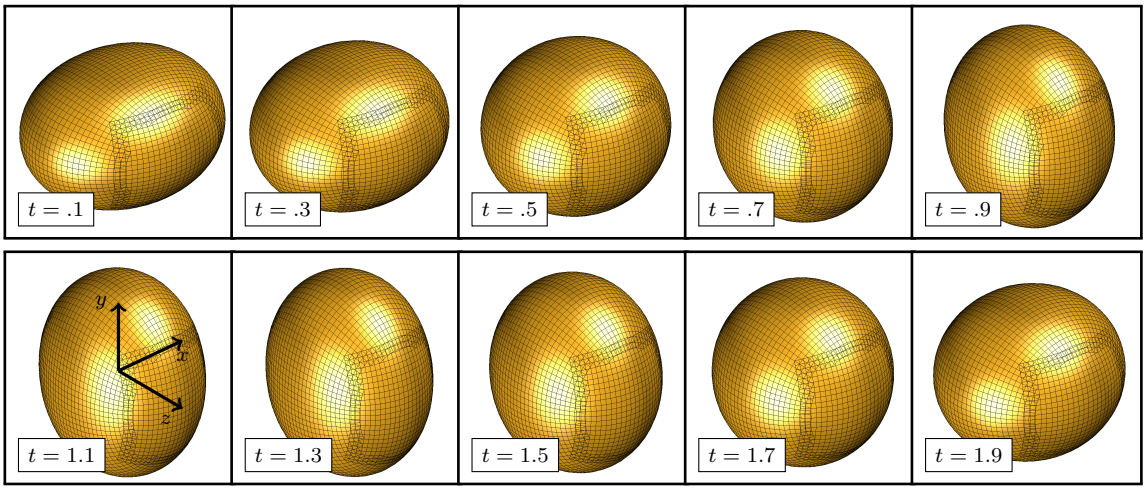

Figure 23: Vibrational mode of an incompressible solid sphere with a traction boundary condition. Computed solutions showing the displacement of the surface at selected times.

Figure 23 shows some computed results for the vibration of a solid sphere with traction boundary conditions, mode $T_{1,2,2}$ in Table 7. The deformed surface is shown at selected times. In this vibrational mode the sphere becomes elongated and shortened primarily along the x and y-axes[10]. Since the material is incompressible, the volume of the sphere remains constant as it deforms. Note

[10]Vibrational modes with $m_\phi = 2$ and zero-traction boundary conditions are called *spheroidal vibrations* in Love [37].

that the north pole is situated at the center of the orthographic patch as seen to the lower right of each deformed sphere.

6.6. Long-time simulations

In this section we perform some very long-time simulations to confirm numerically that the solutions computed using the fractional-step schemes remain stable and bounded. Initial conditions are chosen with random grid values on $[0,1]$ so that all eigenmodes, including any possible unstable ones, would be seeded with an order one amount of energy. The numerical schemes are integrated to very long times and the solutions are monitored for any growth. Due to the upwinding, the magnitude of the computed solutions for a stable scheme are expected to slowly decay to zero over time.

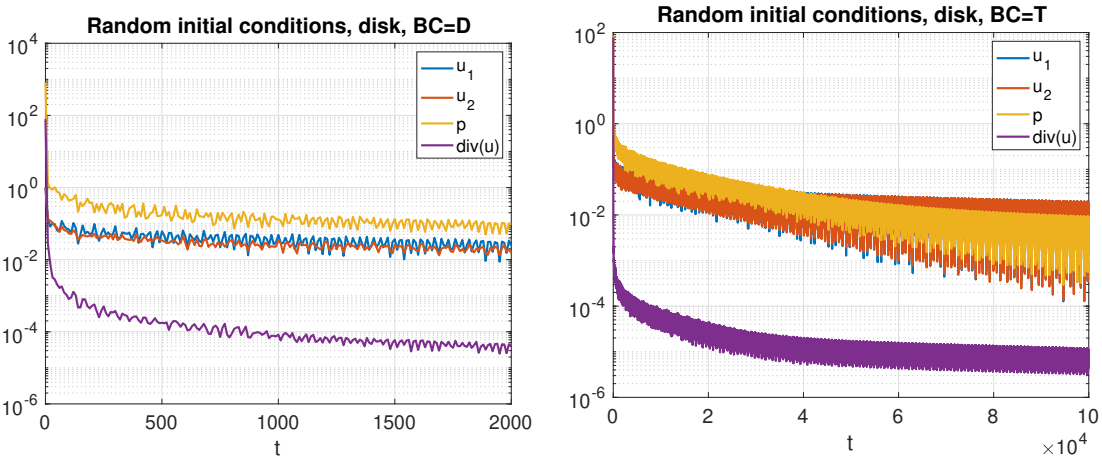

Figure 24: Long-time integration for a disk domain with random initial conditions. Solution norms versus time for BC = D (left) and BC = T (right).

Linear in time null-space mode. For problems with traction or periodic boundary conditions on all boundaries the equations of linear elasticity (5) have nullspace solutions where the pressure is spatially uniform and each component of displacement $u_i(\mathbf{x},t)$ is a linear polynomial in space multiplied by a linear polynomial in time,

$$u_i = (a_{0,i} + a_{1,i}\,x + a_{2,i}\,y + a_{3,i}\,z)\,(b_{0,i} + b_{1,i}\,t), \qquad i = 1,\ldots,n_d, \tag{128}$$

where $\{a_{k,i}\}$ and $\{b_{k,i}\}$ are coefficients. These functions lie in the nullspace of the initial-boundary-value problem provided the coefficients satisfy certain constraints imposed by the boundary conditions, divergence-free condition, and initial conditions. Since the linear-mode solutions in (128) are not an indication of instability we remove them from the solution for the purpose of the numerical tests considered here. The linear modes can be removed by projecting them out after every few hundred time-steps. The coefficients $a_{k,i}$ and $b_{k,i}$ in (128) are estimated at a fixed time from a least-squares fit to the computed solution on the grid, and then this linear mode is subtracted from the discrete solution (e.g. from both the current and previous time-levels for the SOS-ME scheme).

Figure 24 shows results for the disk domain considered in Section 6.3 with random initial conditions. The max-norms of the solution components are graphed versus time. The norms are only plotted at selected times, for example at $t = 10$, 20, 30, etc. The linear-time mode is removed from the solution for case of traction boundary conditions, BC = T. For the case of traction boundary conditions the final time is $t = 10^5$ and this requires approximately 6.8×10^6 time-steps. The norms oscillate as energy is transferred, for example, between the displacement and its time

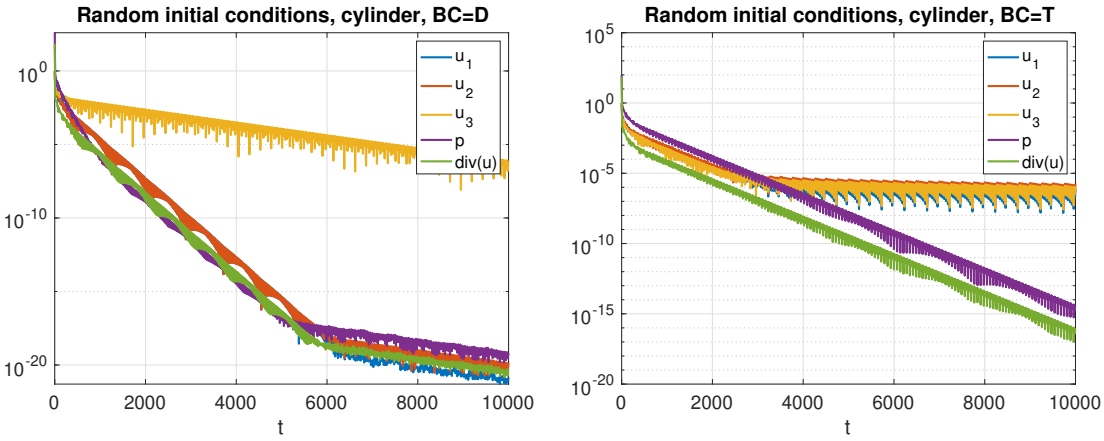

Figure 25: Long-time integration for a cylinder domain with random initial conditions. Solution norms versus time for BC = D (left) and BC = T (right).

derivative, but on average the norms are seen to slowly decay over time. At large times, only smooth modes remain, and these decay very slowly due to the small damping from the upwind dissipation.

Figures 25 and 26 show similar results for a three-dimensional cylinder and three-dimensional sphere with random initial conditions. The linear time mode is again removed from the solution for BC = T. For the cylinder case with traction boundary conditions the simulation is run for approximately 5.7×10^5 time-steps to $t = 10^4$ and no instability is observed.

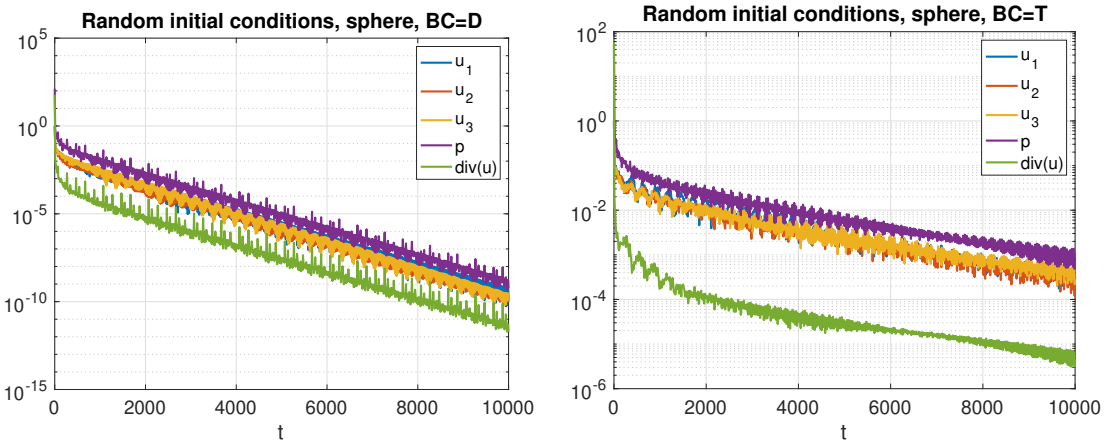

Figure 26: Long-time integration for a sphere domain with random initial conditions. Solution norms versus time for BC = D (left) and BC = T (right).

7. Conclusions

We have described new finite-difference algorithms for solving the equations of incompressible linear elasticity on complex geometry. The governing equations are solved in displacement-pressure form using a fractional-step algorithm that separates the update for the displacement from the solution for the pressure. Upwinding is incorporated, and is essential for stability in the presence of grid interfaces. The upwind approach together with compatibility boundary conditions are also important to ensure stability in the presence of traction boundary conditions. Two second-order

accurate schemes are developed. The first SOS-ME-scheme is a single-step space-time scheme based on the modified equation approach. The second FOT-PC-scheme is a method-of-lines based scheme that uses a predictor-corrector time-stepping scheme for the equations written as a first order system in time for the displacement and velocity. To keep the dilatation small, a divergence damping term is added to the pressure Poisson equation. A von Neumann stability analysis showed the SOS-ME-scheme is stable to a CFL number of one provided the coefficient of divergence damping satisfied a certain bound. A GKS mode analysis of a model IBVP proved the stability of the scheme with displacement and traction boundary conditions, the latter requiring upwind dissipation.

The two schemes were implemented in two and three space dimensions on overset grids. An extensive set of exact solutions for a variety of geometries is obtained, and numerical results for these problems demonstrate the accuracy and stability of schemes. The exact solutions described here also provide a useful set of benchmark problems for the verification of other schemes. In future work we will consider extensions to fourth-order accuracy and nonlinear materials.

Appendix A. Time-step restriction with divergence damping

A proof of Theorem 1 is given in this section. Our goal is to find the time-step restriction for the SOS-ME scheme given by

$$D_{+t}D_{-t}\mathbf{u}_{\mathbf{j}}^n + \frac{1}{\rho}\nabla_h p_{\mathbf{j}}^n = c^2\Delta_h \mathbf{u}_{\mathbf{j}}^n, \tag{A.1a}$$

$$\frac{1}{\rho}\Delta_h p_{\mathbf{j}}^n = \frac{c_d}{\Delta t}\nabla_h \cdot \left(D_{-t}u_{\mathbf{j}}^n\right), \tag{A.1b}$$

discretized to second-order accuracy in space on a Cartesian grid for the periodic domain $\Omega = [0, 2\pi]^{n_d}$. Following a von Neumann stability analysis, we first expand the solution in a discrete Fourier series in space. This leads us to consider the following ansatz for a single Fourier mode as a modal solution to (A.1):

$$\begin{bmatrix} \mathbf{u}_{\mathbf{j}}^n \\ p_{\mathbf{j}}^n \end{bmatrix} = a^n\, e^{i\mathbf{k}\cdot\mathbf{x}_{\mathbf{j}}} \begin{bmatrix} \mathbf{U}_{\mathbf{k}} \\ P_{\mathbf{k}} \end{bmatrix}, \tag{A.2}$$

where a is an amplification factor, $\mathbf{k} = [k_1, k_2, k_3]$ is the wave vector with $k_m = -N_m/2, -N_m/2 + 1, \ldots, N_m/2 - 1$ and $\mathbf{U}_{\mathbf{k}}$ and $P_{\mathbf{k}}$ are Fourier coefficients. Here, N_m specifies the number of grid points in the m-direction and it is assumed to be an even integer for convenience. Substituting (A.2) into (A.1) leads to equations for the Fourier coefficients given by

$$\frac{a - 2 + a^{-1}}{\Delta t^2}\mathbf{U}_{\mathbf{k}} + \frac{1}{\rho}\widehat{\nabla_h} P_{\mathbf{k}} = c^2\widehat{\Delta_h}\mathbf{U}_{\mathbf{k}}, \tag{A.3a}$$

$$\frac{1}{\rho}\widehat{\Delta_h} P_{\mathbf{k}} = \frac{c_d}{\Delta t}\widehat{\nabla_h} \cdot \frac{1 - a^{-1}}{\Delta t}\mathbf{U}_{\mathbf{k}}, \tag{A.3b}$$

where $\widehat{\Delta_h}$ and $\widehat{\nabla_h}$ are the discrete Fourier symbols of Δ_h and ∇_h, respectively, given by

$$\widehat{\Delta_h} \stackrel{\text{def}}{=} -\sum_{m=1}^{n_d} \frac{\sin^2(k_m \Delta x_m/2)}{(\Delta x_m/2)^2}, \tag{A.4}$$

$$\widehat{\nabla_h} \stackrel{\text{def}}{=} \begin{bmatrix} \widehat{D_{0,x}} \\ \widehat{D_{0,y}} \\ \widehat{D_{0,z}} \end{bmatrix} = \begin{bmatrix} i\dfrac{\sin(k_1\Delta x_1)}{\Delta x_1} \\ i\dfrac{\sin(k_2\Delta x_2)}{\Delta x_2} \\ i\dfrac{\sin(k_3\Delta x_3)}{\Delta x_3} \end{bmatrix}. \tag{A.5}$$

Using (A.3b) to eliminate $P_{\mathbf{k}}$ from (A.3a) gives

$$(\hat{s}^2 - c^2\widehat{\Delta_h})\mathbf{U}_{\mathbf{k}} + \alpha \frac{\widehat{\nabla_h}}{\widehat{\Delta_h}}(\widehat{\nabla_h} \cdot \mathbf{U}) = 0, \tag{A.6a}$$

where

$$\hat{s}^2 \stackrel{\text{def}}{=} \frac{a - 2 + a^{-1}}{\Delta t^2}, \tag{A.6b}$$

$$\alpha \stackrel{\text{def}}{=} \frac{c_d}{\Delta t^2}(1 - a^{-1}). \tag{A.6c}$$

Here, and in the following, we ignore the special case of a constant mode in space when $\mathbf{k} = 0$. In this special case the solution is constant in space and the pressure mode $P_{\mathbf{k}}$ is only determined up to a constant; this constant mode does not affect the time-step. Furthermore, note that $-\widehat{\Delta_h} > 0$ for $\mathbf{k} \neq \mathbf{0}$. In matrix form, (A.6a) is

$$\begin{bmatrix} \hat{s}^2 - c^2\widehat{\Delta_h} + \alpha\dfrac{\widehat{D_{0,x}}^2}{\widehat{\Delta_h}} & \alpha\dfrac{\widehat{D_{0,x}}\widehat{D_{0,y}}}{\widehat{\Delta_h}} & \alpha\dfrac{\widehat{D_{0,x}}\widehat{D_{0,z}}}{\widehat{\Delta_h}} \\ \alpha\dfrac{\widehat{D_{0,x}}\widehat{D_{0,y}}}{\widehat{\Delta_h}} & \hat{s}^2 - c^2\widehat{\Delta_h} + \alpha\dfrac{\widehat{D_{0,y}}^2}{\widehat{\Delta_h}} & \alpha\dfrac{\widehat{D_{0,y}}\widehat{D_{0,z}}}{\widehat{\Delta_h}} \\ \alpha\dfrac{\widehat{D_{0,x}}\widehat{D_{0,z}}}{\widehat{\Delta_h}} & \alpha\dfrac{\widehat{D_{0,y}}\widehat{D_{0,z}}}{\widehat{\Delta_h}} & \hat{s}^2 - c^2\widehat{\Delta_h} + \alpha\dfrac{\widehat{D_{0,z}}^2}{\widehat{\Delta_h}} \end{bmatrix} \mathbf{U} = 0. \tag{A.7}$$

The matrix in (A.7) must be singular for nontrivial solutions for $\mathbf{U}$ to exist which leads to the determinant condition

$$\mathcal{D}(a) \stackrel{\text{def}}{=} \left(\hat{s}^2 - c^2\widehat{\Delta_h}\right)^2 \left(\hat{s}^2 - c^2\widehat{\Delta_h} + \frac{\alpha}{\widehat{\Delta_h}}\left(\widehat{D_{0,x}}^2 + \widehat{D_{0,y}}^2 + \widehat{D_{0,z}}^2\right)\right) = 0. \tag{A.8}$$

Equation (A.8) can be viewed as an equation to determine the amplification factor a as a function of $\mathbf{k}$, c, Δt and c_d. The leading two factors in $\mathcal{D}(a)$ (which are of the same form as when solving a scalar wave equation) give roots a satisfying

$$\hat{s}^2 - c^2\widehat{\Delta_h} = 0, \tag{A.9a}$$

and this expression can be used to eliminate $\hat{s}^2$ in (A.6b) leading to a quadratic equation for a given by

$$a^2 - 2\left(1 + \frac{c^2\Delta t^2}{2}\widehat{\Delta_h}\right)a + 1 = 0. \tag{A.9b}$$

Requiring solutions to be bounded in time so that $|a| \leq 1$, and with no double roots when $|a| = 1$, leads to the requirement

$$\frac{c^2\Delta t^2}{2}(-\widehat{\Delta_h}) < 2, \tag{A.10}$$

which must hold for all valid wave numbers $\mathbf{k}$. Finding the worst case wave number leads to the time-step restriction in (36), which is the usual condition for the discretized scalar wave equation. The last factor in (A.8) (which corresponds to a damped wave equation for the divergence) implies that a satisfyies

$$\hat{s}^2 - c^2\widehat{\Delta_h} + \frac{\alpha}{\widehat{\Delta_h}}\big(\widehat{D_{0,x}}^2 + \widehat{D_{0,y}}^2 + \widehat{D_{0,z}}^2\big) = 0, \tag{A.11}$$

or equivalently

$$a^2 - 2\Big(1 + \frac{c^2\Delta t^2}{2}\widehat{\Delta_h} - \frac{\gamma}{2}\Big)a + 1 - \gamma = 0, \tag{A.12a}$$

where

$$\gamma \stackrel{\text{def}}{=} \frac{c_d}{\widehat{\Delta_h}}\Big(\widehat{D_{0,x}}^2 + \widehat{D_{0,y}}^2 + \widehat{D_{0,z}}^2\Big). \tag{A.12b}$$

We now wish to determine conditions on the divergence damping coefficient c_d so that roots, a, of (A.12a) satisfy the root condition under the time-step restriction in (36). When this is the case, the divergence damping does not force a smaller time-step.

The theory of von Neumann polynomials [38] can be used to determine conditions on the coefficients in (A.12a) so that the roots a satisfy $|a| \leq 1$. For a quadratic polynomial of the form $a^2 + c_1 a + c_0$ these conditions are

$$|c_0| < 1, \tag{A.13a}$$
$$|c_1| \leq |1 + c_0|, \tag{A.13b}$$

which, when applied to (A.12a) gives the conditions

$$(1 - \gamma)^2 < 1, \tag{A.14a}$$
$$(2 - \Lambda^2 - \gamma)^2 \leq (2 - \gamma)^2, \tag{A.14b}$$

where

$$\Lambda^2 \stackrel{\text{def}}{=} -c^2\Delta t^2\,\widehat{\Delta_h}. \tag{A.15}$$

To satisfy condition (A.14a) we must satisfy $\gamma < 2$, that is,

$$c_d < 2\frac{\widehat{\Delta_h}}{\widehat{D_{0,x}}^2 + \widehat{D_{0,y}}^2 + \widehat{D_{0,z}}^2} \stackrel{\text{def}}{=} 2\mathcal{R}, \tag{A.16}$$

for all valid $\mathbf{k}$. Using double-angle formulas, e.g. $\sin(k_x\Delta x) = 2\sin(k_x\Delta x/2)\cos(k_x\Delta x/2)$, it is straightforward to show that $\mathcal{R}$ can be written as

$$\mathcal{R} = \frac{\widehat{\Delta_h}}{\widehat{D_{0,x}}^2 + \widehat{D_{0,y}}^2 + \widehat{D_{0,z}}^2} = \frac{S_x^2 + S_y^2 + S_z^2}{S_x^2\,c_x^2 + S_y^2\,c_y^2 + S_z^2\,c_z^2}, \tag{A.17}$$

where

$$S_x \stackrel{\text{def}}{=} \frac{\sin(k_x \Delta x/2)}{\Delta x}, \quad S_y \stackrel{\text{def}}{=} \frac{\sin(k_y \Delta y/2)}{\Delta x}, \quad S_z \stackrel{\text{def}}{=} \frac{\sin(k_z \Delta z/2)}{\Delta x}, \tag{A.18}$$

$$c_x \stackrel{\text{def}}{=} \cos(k_x \Delta x/2), \quad c_y \stackrel{\text{def}}{=} \cos(k_y \Delta y/2), \quad c_z \stackrel{\text{def}}{=} \cos(k_z \Delta z/2). \tag{A.19}$$

Since each factor in the denominator of (A.17) is less than or equal to the corresponding factor in the numerator, it follows that $\mathcal{R} \geq 1$. Whence, we have the necessary requirement that

$$c_d < 2. \tag{A.20}$$

We now must enforce condition (A.14b), which can be rearranged to give

$$c^2 \Delta t^2 \, (-\widehat{\Delta_h}) \leq 2(2 - \gamma). \tag{A.21}$$

Note that γ, defined in (A.12b), can be written in an expanded form as

$$\gamma = c_d - c_d \, \frac{S_x^2 s_x^2 + S_y^2 s_y^2 + S_z^2 s_z^2}{S_x^2 + S_y^2 + S_z^2}, \tag{A.22}$$

where

$$s_x \stackrel{\text{def}}{=} \sin(k_x \Delta x/2), \quad s_y \stackrel{\text{def}}{=} \sin(k_y \Delta y/2), \quad s_z \stackrel{\text{def}}{=} \sin(k_z \Delta z/2). \tag{A.23}$$

Introduce the time-step parameter λ_{CFL} defined by

$$\lambda_{\text{CFL}}^2 \stackrel{\text{def}}{=} c^2 \, \Delta t^2 \left(\frac{1}{\Delta x^2} + \frac{1}{\Delta y^2} + \frac{1}{\Delta z^2} \right). \tag{A.24}$$

We now use the definition for λ_{CFL} in (A.24) to eliminate $c^2 \, \Delta t^2$ in (A.21) to give the requirement

$$\lambda_{\text{CFL}}^2 \leq \frac{2(2 - \gamma)}{-\widehat{\Delta_h}} \left(\frac{1}{\Delta x^2} + \frac{1}{\Delta y^2} + \frac{1}{\Delta z^2} \right) \stackrel{\text{def}}{=} \mathcal{T}. \tag{A.25}$$

Using (A.22) in the above definition for $\mathcal{T}$ to eliminate γ gives

$$\mathcal{T} = \frac{1}{2(S_x^2 + S_y^2 + S_z^2)} \left\{ 2 - c_d + c_d \, \frac{S_x^2 s_x^2 + S_y^2 s_y^2 + S_z^2 s_z^2}{S_x^2 + S_y^2 + S_z^2} \right\} \left(\frac{1}{\Delta x^2} + \frac{1}{\Delta y^2} + \frac{1}{\Delta z^2} \right), \tag{A.26a}$$

$$= \frac{1}{2} \Big\{ (2 - c_d) \mathcal{T}_1 + c_d \mathcal{T}_2 \Big\}, \tag{A.26b}$$

where

$$\mathcal{T}_1 \stackrel{\text{def}}{=} \frac{1}{S_x^2 + S_y^2 + S_z^2} \left(\frac{1}{\Delta x^2} + \frac{1}{\Delta y^2} + \frac{1}{\Delta z^2} \right), \tag{A.26c}$$

and

$$\mathcal{T}_2 \stackrel{\text{def}}{=} \frac{S_x^2 s_x^2 + S_y^2 s_y^2 + S_z^2 s_z^2}{(S_x^2 + S_y^2 + S_z^2)^2} \left(\frac{1}{\Delta x^2} + \frac{1}{\Delta y^2} + \frac{1}{\Delta z^2} \right). \tag{A.26d}$$

We wish to know what the smallest value $\mathcal{T}$ can be. To do this, we first show that $\mathcal{T}_1 \geq 1$ and $\mathcal{T}_2 \geq 1$. The condition $\mathcal{T}_1 \geq 1$ follows from

$$\frac{1}{\Delta x^2} + \frac{1}{\Delta y^2} + \frac{1}{\Delta z^2} \geq \frac{s_x^2}{\Delta x^2} + \frac{s_y^2}{\Delta y^2} + \frac{s_z^2}{\Delta z^2}. \tag{A.27}$$

To show $\mathcal{T}_2 \geq 1$, take the product of the second term and the numerator of the first term, and then expand the denominator, to give

$$\mathcal{T}_2 = \frac{\frac{s_x^4}{\Delta x^4} + \frac{s_z^4}{\Delta z^4} + \frac{s_y^4}{\Delta y^4} + \frac{s_x^4}{\Delta x^2}\left(\frac{1}{\Delta y^2} + \frac{1}{\Delta z^2}\right) + \frac{s_y^4}{\Delta y^2}\left(\frac{1}{\Delta x^2} + \frac{1}{\Delta z^2}\right) + \frac{s_z^4}{\Delta z^2}\left(\frac{1}{\Delta x^2} + \frac{1}{\Delta y^2}\right)}{\frac{s_x^4}{\Delta x^4} + \frac{s_y^4}{\Delta y^4} + \frac{s_z^4}{\Delta z^4} + 2\frac{s_x^2 s_y^2}{\Delta x^2 \Delta y^2} + 2\frac{s_x^2 s_z^2}{\Delta x^2 \Delta z^2} + 2\frac{s_y^2 s_z^2}{\Delta y^2 \Delta z^2}}. \tag{A.28}$$

Since $2s_x^2 s_y^2 \leq s_x^4 + s_y^4$, etc., it follows that $\mathcal{T}_2 \geq 1$. Whence, assuming $0 \leq c_d < 2$, (A.26b) gives

$$\mathcal{T} = \frac{1}{2}\Big\{(2 - c_d)\mathcal{T}_1 + c_d \mathcal{T}_2\Big\} \geq \frac{1}{2}\big\{(2 - c_d) + c_d\big\} = 1. \tag{A.29}$$

Therefore the second von Neumann polynomial condition (A.14b) is satisfied provided

$$\lambda_{\text{CFL}}^2 \leq 1, \tag{A.30}$$

which is the same condition as before. This completes the proof.

Appendix B. Von Neumann analysis of the model problem

In this section we prove Theorem 2. We perform a discrete Fourier transform in space and look for solutions of the form

$$\mathbf{u}_{\mathbf{j}}^n = a^n \, e^{i\mathbf{k}\cdot\mathbf{x}_{\mathbf{j}}} \, \hat{\mathbf{u}}_{\mathbf{k}}, \qquad p_{\mathbf{j}}^n = a^n \, e^{i\mathbf{k}\cdot\mathbf{x}_{\mathbf{j}}} \, \hat{p}_{\mathbf{k}}, \tag{B.1}$$

where a is the amplification factor in time, $\mathbf{k}$ is a wave number, and $\hat{\mathbf{u}}_{\mathbf{k}}$ and $\hat{p}_{\mathbf{k}}$ are Fourier coefficients. We wish to find conditions on Δt such that $|a| \leq 1$ for all valid $\mathbf{k} = [k_x, k_y]$, with $k_d = -N_d/2, -N_d/2 + 1, \ldots, N_d/2 - 1$, assuming N_d an even integer for convenience. From (39c) we find that the pressure satisfies

$$\hat{\Delta}_h \, \hat{p}_{\mathbf{k}} = 0, \tag{B.2}$$

where the scalar $\hat{\Delta}_h$ is the Fourier symbol of Δ_{2h},

$$\hat{\Delta}_h \stackrel{\text{def}}{=} \widehat{D_{+x}D_{-x}} + \widehat{D_{+y}D_{-y}}, \tag{B.3a}$$

$$\widehat{D_{+x}D_{-x}} \stackrel{\text{def}}{=} \frac{-4\sin^2(k_x \Delta x/2)}{\Delta x^2}, \tag{B.3b}$$

$$\widehat{D_{+y}D_{-y}} \stackrel{\text{def}}{=} \frac{-4\sin^2(k_y \Delta y/2)}{\Delta y^2}. \tag{B.3c}$$

Since $\hat{\Delta}_h < 0$ for $\mathbf{k} \neq 0$ it follows that $\hat{p}_{\mathbf{k}} = 0$ if $\mathbf{k} \neq \mathbf{0}$. The constant mode in the pressure when $\mathbf{k} = \mathbf{0}$ is arbitrary and we take it to be zero. From (39a) or (39b) we then find that a must satisfy

$$\frac{a - 2 + a^{-1}}{\Delta t^2} = c^2 \hat{\Delta}_h + c\,\beta\,(\Delta x \widehat{D_{+x}D_{-x}} + \Delta y \widehat{D_{+y}D_{-y}})\frac{1 - a^{-1}}{\Delta t}. \tag{B.4}$$

We are thus led to the following quadratic equation for the amplification factor a,

$$a^2 - 2(1 + z_1/2)a + 1 + z_2 = 0, \tag{B.5a}$$

where

$$z_1 \stackrel{\text{def}}{=} c^2\Delta t^2\,\hat{\Delta}_h + z_2, \tag{B.5b}$$

$$z_2 \stackrel{\text{def}}{=} (c\Delta t)\,\beta(\Delta x\widehat{D_{+x}D_{-x}} + \Delta y\widehat{D_{+y}D_{-y}}). \tag{B.5c}$$

From the theory of von Neumann polynomials we require the two conditions

$$|1 + z_2| < 1, \tag{B.6a}$$

$$(2 + z_1)^2 \leq (2 + z_2)^2 \tag{B.6b}$$

Condition (B.6a) implies $-z_2 < 2$ so that

$$c\Delta t\beta\left(\frac{4\sin^2(k_x\Delta x/2)}{\Delta x} + \frac{4\sin^2(k_y\Delta y/2)}{\Delta y}\right) < 2, \tag{B.7}$$

and this must hold for all valid wave numbers $\mathbf{k}$ which implies

$$c\Delta t\beta\left(\frac{1}{\Delta x} + \frac{1}{\Delta y}\right) < \frac{1}{2}. \tag{B.8}$$

This condition confirms (41) in Theorem 2. Using the definition in (B.5b) to eliminate z_1 in second von Neumann polynomial condition in (B.6b) gives

$$(2 + z_2 + c^2\Delta t^2\,\hat{\Delta}_h)^2 \leq (2 + z_2)^2, \tag{B.9}$$

and this implies

$$c^2\Delta t^2\,(-\hat{\Delta}_h) \leq 2(2 + z_2). \tag{B.10}$$

Whence

$$c^2\Delta t^2\left(\frac{4\sin^2(k_x\Delta x/2)}{\Delta x^2} + \frac{4\sin^2(k_y\Delta y/2)}{\Delta y^2}\right) \leq 2\left[2 - c\Delta t\beta\left(\frac{4\sin^2(k_x\Delta x/2)}{\Delta x} + \frac{4\sin^2(k_y\Delta y/2)}{\Delta y}\right)\right]. \tag{B.11}$$

This last condition must hold for all valid $\mathbf{k}$ which implies

$$c^2\Delta t^2\left(\frac{1}{\Delta x^2} + \frac{1}{\Delta y^2}\right) \leq 1 - 2c\Delta t\beta\left(\frac{1}{\Delta x} + \frac{1}{\Delta y}\right), \tag{B.12}$$

and this condition confirms (40) in Theorem 2. This completes the proof.

References

[1] J. P. Whiteley, Discontinuous Galerkin finite element methods for incompressible non-linear elasticity, Computer Methods in Applied Mechanics and Engineering 198 (41) (2009) 3464–3478.

[2] W. D. Henshaw, A fourth-order accurate method for the incompressible Navier-Stokes equations on overlapping grids, J. Comput. Phys. 113 (1) (1994) 13–25.

[3] W. D. Henshaw, N. A. Petersson, A split-step scheme for the incompressible Navier-Stokes equations, in: M. M. Hafez (Ed.), Numerical Simulation of Incompressible Flows, World Scientific, 2003, pp. 108–125.

[4] F. Meng, J. W. Banks, W. D. Henshaw, D. W. Schwendeman, Fourth-order accurate fractional-step IMEX schemes for the incompressible Navier-Stokes equations on moving overlapping grids, Computer Methods in Applied Mechanics and Engineering 366 (2020) 113040.

[5] A. Ilan, D. Loewenthal, Instability of finite difference schemes due to boundary conditions in elastic media, Geophysical Prospecting 24 (1976) 431–453.

[6] S. Nilsson, N. A. Petersson, B. Sjögreen, H.-O. Kreiss, Stable difference approximations for the elastic wave equation in second order formulation, SIAM Journal on Numerical Analysis 45 (5) (2007) 1902–1936.

[7] D. Appelö, S. Nilsson, N. A. Petersson, B. Sjögreen, A stable finite difference method for the elastic wave equation on complex domains with free surface boundary conditions, in: Proceedings of Waves 2007, Reading, United Kingdom, 2007.

[8] D. Appelö, N. A. Petersson, A stable finite difference method for the elastic wave equation on complex geometries with free surfaces, Communications in Computational Physics 5 (2009) 84–107.

[9] K. Duru, G. Kreiss, K. Mattsson, Stable and high-order accurate boundary treatments for the elastic wave equation on second-order form, SIAM Journal on Scientific Computing 36 (6) (2014) A2787–A2818.

[10] N. A. Petersson, B. Sjögreen, Stable grid refinement and singular source discretization for seismic wave simulations, Communications in Computational Physics 8 (2010) 1074–1110.

[11] L. Zhang, S. Wang, N. A. Petersson, Elastic wave propagation in curvilinear coordinates with mesh refinement interfaces by a fourth order finite difference method, SIAM Journal on Scientific Computing 43 (2) (2021) A1472–A1496.

[12] I. Bijelonja, I. Demirdžić, S. Muzaferija, A finite volume method for incompressible linear elasticity, Computer Methods in Applied Mechanics and Engineering 195 (44) (2006) 6378–6390.

[13] P. Cardiff, I. Demirdžić, Thirty years of the finite volume method for solid mechanics, Archives of Computational Methods in Engineering 28 (2021) 3721–3780.

[14] T. J. Hughes, The Finite Element Method, Dover Publications, 2000.

[15] C. Carstensen, G. Dolzmann, S. Funken, D. Helm, Locking-free adaptive mixed finite element methods in linear elasticity, Computer Methods in Applied Mechanics and Engineering 190 (13) (2000) 1701–1718.

[16] M. Chiumenti, Q. Valverde, C. Agelet de Saracibar, M. Cervera, A stabilized formulation for incompressible elasticity using linear displacement and pressure interpolations, Computer Methods in Applied Mechanics and Engineering 191 (46) (2002) 5253–5264.

[17] J. W. Banks, W. D. Henshaw, D. W. Schwendeman, Deforming composite grids for solving fluid structure problems, J. Comput. Phys. 231 (9) (2012) 3518–3547.

[18] L. Li, W. D. Henshaw, J. W. Banks, D. W. Schwendeman, G. A. Main, A stable partitioned FSI algorithm for incompressible flow and deforming beams, J. Comput. Phys. 312 (2016) 272–306.

[19] J. W. Banks, W. D. Henshaw, A. Kapila, D. W. Schwendeman, An added-mass partitioned algorithm for fluid-structure interactions of compressible fluids and nonlinear solids, J. Comput. Phys. 305 (2016) 1037–1064.

[20] J. W. Banks, W. D. Henshaw, D. W. Schwendeman, Q. Tang, A stable partitioned FSI algorithm for rigid bodies and incompressible flow. Part II: General formulation, J. Comput. Phys. 343 (2017) 469–500.

[21] J. W. Banks, W. D. Henshaw, D. W. Schwendeman, Q. Tang, A stable partitioned FSI algorithm for rigid bodies and incompressible flow. Part I: Model problem analysis, J. Comput. Phys. 343 (2017) 432–468.

[22] J. W. Banks, W. D. Henshaw, D. W. Schwendeman, Q. Tang, A stable partitioned FSI algorithm for rigid bodies and incompressible flow in three dimensions, J. Comput. Phys. 373 (2018) 455–492.

[23] D. A. Serino, J. W. Banks, W. D. Henshaw, D. W. Schwendeman, A stable added-mass partitioned (AMP) algorithm for elastic solids and incompressible flow, J. Comput. Phys. 399 (2019) 1–30.

[24] D. A. Serino, J. W. Banks, W. D. Henshaw, D. W. Schwendeman, A stable added-mass partitioned (AMP) algorithm for elastic solids and incompressible flow: Model problem analysis, SIAM J. Sci. Comput. 41 (4) (2019) A2464–A2484.

[25] J. W. Banks, W. D. Henshaw, Upwind schemes for the wave equation in second-order form, J. Comput. Phys. 231 (17) (2012) 5854–5889.

[26] J. Angel, J. W. Banks, W. D. Henshaw, High-order upwind schemes for the wave equation on overlapping grids: Maxwell's equations in second-order form, J. Comput. Phys. 352 (2018) 534–567.

[27] J. B. Angel, J. W. Banks, A. Carson, W. D. Henshaw, Efficient upwind finite-difference schemes for wave equations on overset grids, SIAM J. Sci. Comput.In press.

[28] C. A. Hobbes, Private communication (1995).

[29] W. D. Henshaw, A high-order accurate parallel solver for Maxwell's equations on overlapping grids, SIAM J. Sci. Comput. 28 (5) (2006) 1730–1765.

[30] D. Appelö, J. W. Banks, W. D. Henshaw, D. W. Schwendeman, Numerical methods for solid mechanics on overlapping grids: Linear elasticity, J. Comput. Phys. 231 (18) (2012) 6012–6050.

[31] J. Angel, J. W. Banks, W. D. Henshaw, M. J. Jenkinson, A. V. Kildishev, G. Kovačič, L. J. Prokopeva, D. W. Schwendeman, A high-order accurate scheme for Maxwell's equations with a generalized dispersion model, J. Comput. Phys. 378 (2019) 411–444.

[32] H.-O. Kreiss, Stability theory of difference approximations of mixed initial boundary value problems. I, Mathematics of Computation 22 (1968) 703–714.

[33] B. Gustafsson, H.-O. Kreiss, A. Sundström, Stability theory of difference approximations for mixed initial boundary value problems. II, Mathematics of Computation 26 (119) (1972) 649–686.

[34] J. W. Banks, B. Buckner, W. D. Henshaw, M. J. Jenkinson, A. V. Kildishev, G. Kovačič, L. J. Prokopeva, D. W. Schwendeman, A high-order accurate scheme for Maxwell's equations with a generalized dispersive material (GDM) model and material interfaces, J. Comput. Phys. 412 (2020) 109424.

[35] G. S. Chesshire, W. D. Henshaw, Composite overlapping meshes for the solution of partial differential equations, J. Comput. Phys. 90 (1) (1990) 1–64.

[36] W. D. Henshaw, Ogen: An overlapping grid generator for Overture, Research Report UCRL-MA-132237, Lawrence Livermore National Laboratory (1998).

[37] A. E. H. Love, A Treatise on the Mathematical Theory of Elasticity, Dover Publications, New York, 1944.

[38] J. C. Strikwerda, Finite Difference Schemes and Partial Differential Equations, Wadsworth and Brooks/Cole, 1989.